NASA TECHNICAL NOTE

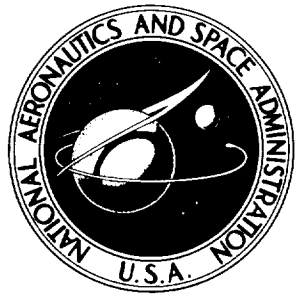

N73-30243
NASA TN D-7275

NASA TN D-7275

LOADING AND HEATING OF A LARGE FLAT PLATE AT MACH 7 IN THE LANGLEY 8-FOOT HIGH-TEMPERATURE STRUCTURES TUNNEL

by William D. Deveikis and L. Roane Hunt

Langley Research Center
Hampton, Va. 23665

NATIONAL AERONAUTICS AND SPACE ADMINISTRATION • WASHINGTON, D. C. • SEPTEMBER 1973

1. Report No. NASA TN D-7275	2. Government Accession No.	3. Recipient's Catalog No.
4. Title and Subtitle LOADING AND HEATING OF A LARGE FLAT PLATE AT MACH 7 IN THE LANGLEY 8-FOOT HIGH-TEMPERATURE STRUCTURES TUNNEL		5. Report Date September 1973 6. Performing Organization Code
7. Author(s) William D. Deveikis and L. Roane Hunt		8. Performing Organization Report No. L-8760
9. Performing Organization Name and Address NASA Langley Research Center Hampton, Va. 23665		10. Work Unit No. 502-32-01-01 11. Contract or Grant No.
12. Sponsoring Agency Name and Address National Aeronautics and Space Administration Washington, D.C. 20546		13. Type of Report and Period Covered Technical Note 14. Sponsoring Agency Code

15. Supplementary Notes

16. Abstract

Surface pressure and cold-wall heating-rate distributions (wall-temperature to total-temperature ratio approximately 0.2) were obtained on a large, flat calibration panel at a nominal Mach number of 7 in the Langley 8-foot high-temperature structures tunnel. Panel dimensions were 108.0 by 152.4 cm (42.5 by 60.0 in.). Test objectives were (1) to map available flat-plate loading and heating provided by the facility and (2) to determine effectiveness of leading-edge bluntness, boundary-layer trips, and aerodynamic fences in generating a uniform, streamwise turbulent flow field over the test surface of a flat-sided panel holder. Tests were conducted at angles of attack to 15^{o} for free-stream unit Reynolds numbers from 1.240×10^{6} to 5.545×10^{6} per meter (0.378×10^{6} to 1.69×10^{6} per foot), at stagnation pressures between 4.275 and 18.06 MPa (620 and 2620 psia), and at stagnation temperatures of 1400 K (2500^{o} R) and 1900 K (3400^{o} R) in a products-of-combustion test medium.

17. Key Words (Suggested by Author(s))	18. Distribution Statement
Hypersonic Flat plate Heating Pressure Boundary-layer transition	Unclassified – Unlimited

19. Security Classif. (of this report)	20. Security Classif. (of this page)	21. No. of Pages	22. Price*
Unclassified	Unclassified	67	Domestic, $3.50 Foreign, $6.00

*For sale by the National Technical Information Service, Springfield, Virginia 22151

LOADING AND HEATING OF A LARGE FLAT PLATE AT MACH 7 IN THE LANGLEY 8-FOOT HIGH-TEMPERATURE STRUCTURES TUNNEL

By William D. Deveikis and L. Roane Hunt
Langley Research Center

SUMMARY

Surface pressure and cold-wall heating-rate distributions (wall-temperature to total-temperature ratio approximately 0.2) were obtained on a large, flat calibration panel at a nominal Mach number of 7 in the Langley 8-foot high-temperature structures tunnel. Panel dimensions were 108.0 by 152.4 cm (42.5 by 60.0 in.). Test objectives were (1) to map available flat-plate loading and heating provided by the facility and (2) to determine effectiveness of leading-edge bluntness, boundary-layer trips, and aerodynamic fences in generating a uniform, streamwise turbulent flow field over the test surface of a flat-sided panel holder. Tests were conducted at angles of attack to 15° for free-stream unit Reynolds numbers from 1.240×10^6 to 5.545×10^6 per meter (0.378×10^6 to 1.69×10^6 per foot), at stagnation pressures between 4.275 and 18.06 MPa (620 and 2620 psia), and at stagnation temperatures of 1400 K (2500° R) and 1900 K (3400° R) in a test medium comprising combustion products of methane and air.

The results indicated that surface pressures from 0.90 to 15.2 kPa (0.13 to 2.20 psia) and cold-wall turbulent heating rates from 29.5 to 250 kW/m^2 (2.6 to 22.0 Btu/ft^2-sec) are available in the present range of test conditions. Average pressures were predicted within ±10 percent using oblique-shock relations, and average heating rates were overpredicted from 10 to 30 percent using Eckert's reference temperature, as was expected for the present wall-temperature to total-temperature ratio. Other results showed that with a sharp leading edge, Mach number distributions normal to the surface were more uniform than were obtained with a blunt leading edge; boundary-layer trips generated fully turbulent flow uniformly in the spanwise direction within ±5 percent over the panel surface at all angles of attack and Reynolds numbers; and aerodynamic fences diminished the tendency of flow streamlines to deflect with angle of attack over the panel surface and, hence, improved pressure distributions.

INTRODUCTION

Environmental testing has become an essential element in resolving many of the structural problems associated with flight at hypersonic speeds that are important to

the development of the structural design technology for efficient operation of flight structures in the hypersonic environment (ref. 1). In this regard, the Langley 8-foot high-temperature structures tunnel (ref. 2) was conceived for evaluating the aeroelastic, structural, and thermal performance of full-scale components of advanced structural design concepts in a simulated aerodynamic loading and heating environment comparable to flight at Mach 7. One of the major technology areas scheduled for investigation in this facility is the surface structure and thermal control system for hypersonic vehicles. For this work, a flat-sided panel holder that can accommodate full-scale prototype surface structure panel concepts was constructed. However, before tests of these concepts could begin, a detailed definition of the pressure and heating-rate distributions that would be encountered over the test surface was first required. Thus, the present investigation was undertaken to obtain base-line data on available aerodynamic loading and heating by using a flat calibration panel 108.0 by 152.4 cm (42.5 by 60.0 in.) mounted on the panel holder.

For these tests, it was of interest to subject the panel both to uniform pressure loading and to turbulent heating. The former required a flow field free of cross flow, whereas the latter required fixing the location of boundary-layer transition ahead of the panel. Consequently, as part of this investigation, the effectiveness of leading-edge bluntness and boundary-layer trip height in generating fully turbulent flow and the effectiveness of aerodynamic fences in providing a uniformly distributed streamwise flow over the panel surface were evaluated.

Distributions of cold-wall aerodynamic heating rates for a wall-temperature to total-temperature ratio of approximately 0.2, static pressures on the panel surface, and pitot pressures above the surface were obtained for angles of attack up to 15^{o}, for stagnation temperatures of 1400 K (2500^{o} R) and 1900 K (3400^{o} R), and for a range of total pressures that yielded free-stream unit Reynolds numbers between 1.240×10^{6} and 5.545×10^{6} per meter (0.378×10^{6} and 1.69×10^{6} per foot). The test medium was the combustion products of methane and air which, as reported in reference 2, provides aerodynamic pressure and heating coefficients comparable to those obtained in test facilities using air. Measured pressure and heating distributions are compared with theoretical distributions, and carpet plots summarizing the heating and loading results are presented.

SYMBOLS

Although physical quantities were measured in U.S. Customary Units, they are presented in this paper in the International System of Units (SI). Factors relating the two systems are given in reference 3 and in the appendix.

c_p	specific heat at constant pressure
h	vertical distance from tunnel center line, m (in.)
l	longitudinal distance from nozzle exit (see fig. 4), m (in.)
M	Mach number
N_{Pr}	Prandtl number
R	Reynolds number based on x
R_L	unit Reynolds number, per meter (per foot)
N_{St}	Stanton number
p	pressure, Pa (psia)
q	heating rate, W/m^2 (Btu/ft^2-sec)
T	temperature, K (^oR)
t	time, sec
V	velocity
w	width of panel holder, m (in.)
x,y,z	coordinates of panel holder (see fig. 1), m (in.)
α	angle of attack, deg
ρ	density
τ	thickness

Superscripts:

'	pitot
*	Eckert's reference temperature

Subscripts:

aw	adiabatic wall
cl	center line
l	local
t	total condition in combustor
w	wall
1	blunt leading edge
2	sharp leading edge
∞	free stream

APPARATUS AND TESTS

Panel Holder

The present tests were conducted using the panel holder illustrated in figure 1. Its basic configuration was that of a rectangular slab with a 20° bevel at the leading edge, as shown in figure 1(a). A large rectangular cutout through the panel holder could accommodate test-panel sizes up to 108.0 by 152.4 cm (42.5 by 60.0 in.) with access to the back of the test panel by means of a removable plate on the back surface of the panel holder (fig. 1(b)). Construction of the panel holder was of 2.54-cm-thick (1-in.) stainless-steel members welded as a framework substructure covered with a protective exterior insulation blanket of 2.54-cm-thick (1-in.) Glasrock foam tiles which were bonded to the substructure. The tiles were ground to provide a test surface that was as flat as possible, but surface conditions varied as a result of the porosity of the Glasrock material and frequent replacement of damaged tiles.

Initially, the leading edge of the panel holder was blunt, and the panel-holder width (designated w_1 in fig. 1(b)) was 147.3 cm (58.0 in.). In subsequent tests, the leading edge of the panel holder was sharp; and for these tests, the Glasrock insulation along both sides of the panel holder was removed, which decreased the panel-holder width (designated w_2 in fig. 1(b)) to 140.7 cm (55.4 in.). The blunt leading-edge configuration is illustrated in figure 1(c). Its radius was 0.96 cm (0.38 in.), and it was constructed of copper with internal passageways for water cooling. The sharp leading-edge configuration

is shown in figure 1(d). This part was constructed of solid stainless steel with a thickness at the leading edge of 0.05 cm (0.02 in.). Its length was shorter than that of the blunt leading edge by the length of the blunt leading-edge radius. With this leading edge, a gap of up to 0.16 cm (0.06 in.) was present between the mating surfaces of the steel leading edge and the Glasrock as a result of irregularities along the upstream edge of the Glasrock.

Two boundary-layer trip sizes were used with the sharper leading edge, namely 0.24- or 0.48-cm-diameter (0.094- or 0.19-in.) stainless-steel spheres, laterally spaced at intervals of 4 trip diameters across the width of the panel-holder test surface. The spheres were located 12.7 cm (5.0 in.) downstream from the leading edge (fig. 1(d)). Trip sizes and lateral spacings were based on criteria of references 4 and 5 which indicate that for a Mach number of 6, a trip height from 1.5 to 3 times the total boundary-layer thickness, and a lateral spacing of 4 times the trip diameter are required to fix the location of boundary-layer transition near the trip across the test surface. For the present investigation, the trips were sized to about 3 times the estimated total boundary-layer thickness expected over the range of test conditions. Although a large pressure drag is associated with such large roughness elements, this effect was not important to the present investigation since only the promotion of turbulent heating was of interest. Other flow distortions produced by the trips conceivably would dissipate over the long distance between the trips and the leading edge of the calibration panel (See ref. 6.)

For the tests with aerodynamic fences, the fence configuration illustrated in figure 1(e) was used. This configuration was developed from 1/12-scale model tests conducted in a hot stream and utilizing oil-flow and schlieren techniques. When attached to the panel holder, the fence extended 7.6 cm (3.0 in.) above the test surface and 25.4 cm (10.0 in.) below the back surface of the panel holder. The fences were constructed from 1.11-cm-thick (0.44-in.) mild steel plate with edges on the exterior surface beveled 30^{o}, as shown in figure 1(e), to allow formation of an attached shock wave. The surface adjacent to the Glasrock test surface was unbeveled.

Calibration Panel

The calibration panel was constructed of Hastelloy X plate which was 0.318 cm (0.125 in.) thick. Its surface roughness was 1.6 μm (64 μin.), rms. The back surface of the panel was insulated by a 3.18-cm-thick (1.25-in.) layer of Glasrock to minimize radiation losses to the interior of the panel holder. In order to minimize warping, the panel was bolted at 156 locations to eleven 7.62-cm (3-in.) I-beams spaced at 15.24-cm (6-in.) intervals across the width of the cutout. All but one of these locations were floating attachments to allow inplane thermal expansion. Assembled in this manner, the panel

surface waviness varied within ±0.6 mm (±0.025 in.) over a minimum wavelength of approximately 76.2 cm (30 in.). In the panel holder, the surface of the panel was flush with the surrounding Glasrock surface. An average gap of 0.3 cm (0.1 in.) between the panel edges and the walls of the rectangular cutout was provided for thermal expansion within the plane of the panel.

Instrumentation

Instrumentation for the calibration panel consisted of 27 surface pressure orifices and 59 chromel-alumel thermocouples whose individual lead wires were spotwelded to the back surface of the panel. The orifices and thermocouples were distributed as shown in figure 2, and inplane locations are listed in table I. The longitudinal coordinate x is measured from the tip of the blunt leading edge (see fig. 1(c)).

A survey rake with eight pitot probes for determining local Mach numbers outside the viscous boundary layer was located near the downstream edge of the calibration panel or 259.8 cm (102.3 in.) from the leading edge of the panel holder (fig. 1(a)). For the present tests, pitot pressures were surveyed at four locations between 2.54 and 10.16 cm (1 and 4 in.) above the Glasrock surface. Static and pitot pressures were measured with the aid of strain-gage pressure transducers located under the calibration panel and connected to 0.15-cm (0.060-in.) inside diameter stainless-steel orifice tubing.

Test Facility

The present tests were conducted in the Langley 8-foot high-temperature structures tunnel which is shown schematically in figure 3. This facility is a hypersonic blowdown wind tunnel which operates at a nominal Mach number of 7, at total pressures between 3.4 and 24.1 MPa (600 and 3500 psia), and at nominal total temperatures between 1400 K and 2000 K (2500° R and 3600° R). Corresponding free-stream unit Reynolds numbers are between 1×10^6 and 10×10^6 per meter (0.3×10^6 and 3.0×10^6 per foot). These conditions simulate the aerothermal flight environment at Mach 7 in the altitude range between 25 and 40 km (80 000 and 130 000 ft).

The high-energy test medium is the products of combustion of a mixture of methane and air which is burned within a pressurized combustion chamber. The combustion products are then expanded to the test-section Mach number by means of an axisymmetric contoured nozzle having an exit diameter of 2.4 m (8 ft). In the test section, the stream is a free jet with a usable test core approximately 1.2 m (4 ft) in diameter over a length of 4.3 m (14 ft) and then enters a straight tube diffuser where it is pumped to the atmosphere by means of a single-stage annular air ejector. Stagnation temperature is controlled by regulating the fuel-to-air ratio.

A cross-sectional view showing various model positions in the test section is presented in figure 4. Models are kept out of the stream until hypersonic flow conditions are established. The model is then inserted rapidly into the stream on an elevator and programed through a sequence of events prescribed by test requirements. Prior to terminating a test, the model is withdrawn from the stream before tunnel shutdown.

Representative variations in pitot and static pressures normalized with respect to stagnation pressure and corresponding free-stream Mach number variations obtained from surveys of the test stream are presented in figure 5. The data shown were obtained in the vertical center-line plane across a stream width of 1 m (40 in.) at two longitudinal stations for a total pressure of 6.9 MPa (1000 psia) and at a total temperature of 1833 K (3300° R). These results indicate that the pitot and static pressures varied within ±9 percent, both vertically and longitudinally. The free-stream Mach numbers determined from these pressures varied within ±3 percent vertically and within ±2 percent longitudinally. Similar variations were observed at higher total pressures.

Tests

The present investigation was conducted in two separate series of tests: one series used the blunt leading edge and the other series used the sharper leading edge. In the former series, the calibration panel faced down as in the photograph of figure 6, whereas in the latter series, the calibration panel faced up as in the photograph of figure 7. The downward facing panel orientation was chosen to minimize the risk of precipitating tunnel flow breakdown during insertion of the panel holder into the test stream. The upward facing panel orientation was imposed on the latter series of tests to correspond to the orientation planned for future tests of surface structure panels that required preheating from above. The panel holder was sting-mounted at its base, and when it was in the test stream at zero angle of attack, the test surface lay 0.15 m (0.5 ft) off the tunnel axis for both panel orientations (fig. 4). In this attitude, the leading edge of the panel holder was located 0.381 m (1.25 ft) downstream from the nozzle exit.

Aerodynamic surface pressures and heating rates were surveyed by pitching the calibration panel into the test stream at different angles of attack over a range of stagnation pressures. Panel insertion was very rapid to provide, as nearly as possible, a step-function exposure to the aerothermal environment. For each exposure, both α and the stagnation pressure were generally held constant. Since cold-wall heating rates were of interest, the calibration panel was at near ambient temperature on insertion and remained in the test stream only about 5 seconds – long enough to ensure that outputs of the pressure transducers had stabilized. However, during test 14 (table II), the panel holder was permitted to sweep through a range of α until flow breakdown occurred.

Test conditions and panel-holder configuration information are summarized in table II for every test. Of the 31 tests that were conducted, the first 10 were on the panel holder with the blunt leading edge. For those tests, the calibration panel was subjected to four nominal total pressures over the operating range of the tunnel and to total temperatures of about 1900 K (3400° R). Corresponding free-stream unit Reynolds numbers at these conditions were nominally 1.3×10^6, 2.0×10^6, 3.3×10^6, and 4.9×10^6 per meter (0.4×10^6, 0.6×10^6, 1.0×10^6, and 1.5×10^6 per foot). However, angle of attack was limited at each total pressure by the range of the surface-pressure transducers, which was from 0 to 7 kPa (0 to 1 psia). In the test series using the sharp leading edge (tests 11 to 31, table II), the calibration panel was instrumented with transducers that sensed pressures up to 35 kPa (5 psia), which permitted testing at α up to at least 15° at all total pressures. Tests 11 to 18 were conducted to observe effects of boundary-layer trip size, and in tests 19 to 31, small boundary-layer trips were used and aerodynamic fences were attached. This latter panel-holder configuration is herein called modified panel holder. In tests 19 to 29, the calibration panel was subjected to only three nominal total pressures and to total temperatures of about 1900 K (3400° R), for which the nominal free-stream Reynolds numbers correspond to the three highest values in the test series without aerodynamic fences. Tests 30 and 31 were conducted near the lower total-temperature limit of 1400 K (2500° R) and at a total pressure of 17.65 MPa (2560 psia) for which the corresponding nominal free-stream unit Reynolds number was 5.40×10^6 per meter (1.65×10^6 per foot).

Data Reduction and Analysis

Outputs from the pressure transducers and thermocouples on the calibration panel were recorded at a sampling rate of 20 per second and were reduced to useful form at the Langley central digital data recording facility. The experimental and analytical quantities reported herein were based on the thermal, transport, and flow properties of the combustion-products test medium as determined from reference 7. Free-stream conditions in the test section were determined from reference measurements in the combustor (fig. 3) by using results from tunnel stream-survey tests such as in figure 5.

Experimental pressure ratios.- All experimentally determined surface pressures were normalized with respect to corresponding free-stream static pressures from table II. The ratio of pitot pressures given by the survey rake to the surface pressure at an orifice located 15 cm (6 in.) upstream of the probes was used to evaluate Mach numbers.

Predicted pressures and Mach numbers.- Theoretical values of local pressures and Mach numbers at the outer edge of the boundary layer were based on the assumption that center-line pressure distributions were constant over the length of the calibration panel as given by the oblique-shock relations of reference 8. For the panel holder with

the sharp leading edge, the local Mach number was obtained directly from oblique-shock relations; whereas, for the panel holder with the blunt leading edge, the local Mach number was calculated by assuming that a normal shock loss occurred across the detached shock wave at the leading edge and that the flow expanded isentropically from the stagnation line to the local pressure given by oblique-shock relations. Additional calculations of center-line pressures and variations in Mach number normal to the surface of the panel with the blunt leading edge were made with the aid of the Lockheed inlet program of reference 9, which utilizes the method of characteristics to account for some leading-edge effects and has been modified to include properties of the combustion-products test medium.

Experimental cold-wall heating rates.- Experimentally determined cold-wall heating rates were evaluated from the one-dimensional heat-balance equation for a thin wall

$$q = \rho c_p \tau \frac{\Delta T}{\Delta t}$$

using the slope of the thermocouple temperature-time variation $\Delta T/\Delta t$ selected at a time very early in the test when effects from thermal conduction and radiation were minimal. Use of the thin-wall technique was justified despite the panel thickness of 0.318 cm (0.125 in.) inasmuch as heating rates so obtained agreed with values that were determined using a finite-difference analysis (ref. 10) for heat transfer through a thick wall. The heating rates determined in this manner were then converted to the nondimensional Stanton number based on the free-stream conditions of table II

$$N_{St,\infty} = \frac{q}{(T_{aw} - T_w)(\rho V c_p)_\infty}$$

Adiabatic-wall temperature T_{aw} was based on reference temperature and laminar and turbulent recovery factors of $\left(N^*_{Pr,l}\right)^{1/2}$ and $\left(N^*_{Pr,l}\right)^{1/3}$, respectively. In order to convert these Stanton numbers to values based on local conditions, the local pressure and local temperature at the outer edge of the boundary layer were assumed constant along the calibration panel and were determined from oblique-shock relations according to the leading-edge configuration, as indicated earlier. Values of local pressure p_l, local temperature T_l, adiabatic-wall temperature T_{aw}, and Eckert's reference temperature T^* (ref. 11) are presented in table III for each test. Conversion factors are also included in table III for determining Stanton numbers based on local free-stream conditions $N_{St,l}$, and on reference temperature conditions $N^*_{St,l}$. The local Reynolds number was based on constant flow conditions along the panel, and the free-stream unit Reynolds number given in table II can be converted to local Reynolds numbers at a distance x from the leading edge of the panel holder by applying the conversion factors of table III.

Calculated cold-wall heating rates.- Analytically determined heating rates were obtained from the relations

$$N^*_{St,\ell} = 0.322\left(N^*_{Pr,\ell}\right)^{-2/3}\left(R^*_\ell\right)^{-1/2}$$

$$N^*_{St,\ell} = 0.0296\left(N^*_{Pr,\ell}\right)^{-2/3}\left(R^*_\ell\right)^{-1/5}$$

for laminar and turbulent boundary layers, respectively. These relations were also based on Eckert's reference temperature and are described in reference 12.

RESULTS AND DISCUSSION

Panel Holder With Blunt Leading Edge

Pressure distributions.- All of the pressure data obtained from tests 1 to 10 (table II) are presented in figure 8. Longitudinal and spanwise distributions of pressures normalized with respect to the free-stream static pressure are plotted as a function of distance normalized with respect to the panel-holder width w_1 for four free-stream unit Reynolds numbers and α up to 15^o. These results indicate that aerodynamic loading was nonuniformly distributed at all test conditions and varied with α. Surface distributions based on figure 8(c) are pictorially represented at $\alpha = 0^o$ and 10^o in figure 9 and illustrate the typical variations obtained. Along the center region of the panel surface, pressures were relatively uniform; but near the trailing-edge corners, the pressures either increased as at $\alpha = 0^o$ in figure 9(a) or decreased when $\alpha > 0^o$ as in figure 9(b) from effects of vortical flow around the sides of the panel holder. Thus at $\alpha = 0^o$, pressures increased near the trailing-edge corners from vortical flow spilling over from higher pressures on the back surface of the panel holder. At $\alpha = 10^o$, the vortical flow was from higher pressures on the test surface; pressures on the calibration panel, therefore, decreased toward the trailing-edge corners. The maximum spanwise change in pressure from the center-line value observed near the trailing edge was approximately 29 percent at $\alpha = 0^o$ and was approximately 16 percent at $\alpha = 15^o$.

In figure 10, the center-line pressure distributions obtained at all angles of attack and free-stream unit Reynolds numbers are plotted as a function of free-stream Reynolds number based on x and are compared with theoretical predictions from references 8 and 9. At $\alpha = 0^o$ for the three lower free-stream unit Reynolds numbers, the pressure along the center line decreased from the leading edge of the panel as a result of effects of flow expansion from the blunt leading edge. The rising pressures toward the trailing edge for the lowest free-stream unit Reynolds number denote boundary-layer separation from flow interference with the sting mount (recall that the panel faced downward in this series

of tests). At $\alpha = 4.5^{\circ}$ and 10°, the pressures tended to increase gradually along the panel length. Local pressure variations generally were within ±3 percent. At $\alpha = 0^{\circ}$, the theory of reference 8 (oblique-shock relations) does not account for bluntness-induced pressure effects and, therefore, predicts a constant value. However, the theory of reference 9 predicts the data at $\alpha = 0^{\circ}$ within ±15 percent. For $\alpha > 0^{\circ}$, the data were within ±15 percent of both theories.

Heating-rate distributions.- All of the thermocouple data obtained from tests 1 to 10 (table II) are presented in figure 11. Longitudinal and spanwise distributions of cold-wall Stanton numbers based on free-stream conditions are plotted as a function of distance normalized with respect to the panel-holder width w_1 for four free-stream unit Reynolds numbers and α up to 15°. These results indicate corresponding α-dependent effects of vortical flow on aerodynamic heating distributions over the panel surface, as shown by the pictorial representations for $\alpha = 0^{\circ}$ and 10° in figure 12 and based on the data of figure 11(b). Thus, at $\alpha = 0^{\circ}$ (fig. 12(a)), heating rates were relatively low over most of the panel surface but increased markedly along the side edges from vortical-flow impingement. At $\alpha = 10^{\circ}$ (fig. 12(b)), the heating rates increased toward the trailing edge over the entire panel surface but were highest along the side edges from boundary-layer disturbances in the presence of vortical cross flow. Stanton numbers varied in the spanwise direction as much as an order of magnitude from the center-line value at $\alpha = 0^{\circ}$ $\left(\text{fig. 11(b)}, \frac{x}{w_1} = 1.686\right)$ and as much as 3 times the center-line value at other values of α $\left(\text{fig. 11(c)}, \frac{x}{w_1} = 0.752\right)$. Results from analysis of data obtained near the center line $\left(\frac{y}{w_1} = -0.021\right)$ and presented in figure 13 showed that these heating-rate variations were produced by variations in the type of boundary layer which, for this case, was either laminar or transitional. In this figure, experimentally determined cold-wall Stanton numbers are plotted as a function of Reynolds number and are compared with curves for laminar and turbulent heating obtained from the relations of reference 12. The Stanton and Reynolds numbers are based on local conditions and Eckert's reference temperature. Laminar heating rates are indicated over the panel length for the two lowest free-stream unit Reynolds numbers at $\alpha = 0^{\circ}$ (circle and square symbols, fig. 13(a)) and lie about 10 percent below the curve for laminar heating. The very low values of Stanton numbers shown by the circle and square symbols at $\alpha = 0^{\circ}$ in figure 13(a) were obtained in the separated-flow region discussed earlier. Transitional heating occurred at the other free-stream unit Reynolds numbers and α as indicated by the rising data. At a given location on the surface, the transitional heating rates increased both with α and free-stream unit Reynolds number and approached fully turbulent values.

However, for the set of data shown by the triangle symbols for $\alpha = 0^{\circ}$ at the highest free-stream unit Reynolds number in figure 13(a), boundary-layer transition apparently occurred prematurely from some unknown disturbance located upstream of the panel.

Modified Panel Holder

Pressure distributions.- All of the pressure data obtained from tests 19 to 29 (table II) are presented in figure 14. Longitudinal and spanwise distributions of pressure ratios are plotted as a function of distance normalized with respect to the panel-holder width w_2 for three free-stream unit Reynolds numbers and α up to 15^o. The data were obtained with the smaller boundary-layer trip diameter (0.24 cm (0.094 in.)) on the sharp leading edge and with aerodynamic fences along the sides of the panel holder. These results show that for $R_{L,\infty} > 2.0 \times 10^6$ per meter (0.6×10^6 per foot), effects of vortical flow on pressures near the trailing-edge corners were not present at $\alpha = 0^o$. For all other conditions, the same α-dependent effects on pressures occurred near the trailing-edge corners to the same extent as encountered on the original panel-holder configuration.

Pictorial representations of surface distributions based on figure 14(b) for $\alpha = 0^o$ and 10^o are presented in figure 15 and illustrate major characteristic differences in surface loading that occurred between the two panel-holder configurations. Thus for $R_{L,\infty} > 2.0 \times 10^6$ per meter (0.6×10^6 per foot), pressures obtained with the modified panel-holder configuration did not increase toward the trailing-edge corners at $\alpha = 0^o$; pressures on the front half of the panel decreased toward the center line slightly at all values of α; and at station $\frac{x}{w_2} = 1.477$, pressures were always about 10 percent higher on one side $-y/w_2$ of the center line than on the other.

As shown in figure 16, pressures along the center line tended to increase gradually over the panel length by about 10 percent at all angles of attack and Reynolds numbers and showed no evidence of expanding flow from the leading edge at $\alpha = 0^o$, as occurred on the panel with the original panel-holder configuration. In this figure, the center-line pressure distributions are plotted as a function of free-stream Reynolds number based on x at all α and unit Reynolds numbers and are compared with predicted values from oblique-shock relations (ref. 8). Local pressure variations were within ± 8 percent, and experimental and predicted values were within ± 15 percent.

Heating-rate distributions.- All of the thermocouple data obtained from tests 19 to 29 (table II) are presented in figure 17. Longitudinal and spanwise distributions of cold-wall Stanton numbers based on free-stream conditions are plotted as a function of distance normalized with respect to the panel width w_2 for three free-stream unit Reynolds numbers and α up to 15^o. These data were obtained using the smaller boundary-layer trip diameter (0.24 cm (0.094 in.)) on the sharp leading edge and with aerodynamic fences along the sides of the panel holder. Turbulent heating rates were obtained over the panel surface at all test conditions except at $\alpha = 0^o$ for the two lower free-stream unit Reynolds numbers shown in figures 17(a) and 17(b). For these conditions, the heating was transitional, as indicated by the rising data along the panel length. As is shown in a subsequent

section, larger boundary-layer trips are required for turbulent heating at the lower free-stream unit Reynolds numbers. The turbulent heating rates varied in the spanwise direction within ±5 percent and characteristically decreased longitudinally by about 15 percent.

Pictorial representations of the surface heating based on figure 17(c) are presented in figure 18 at $\alpha = 0^{\circ}$ and 10° to illustrate the flatter heating distributions that are obtained over the panel surface when transitional heating is not present. The level of heating shown was fully turbulent, as deduced from the data obtained near the center line $\left(\frac{y}{w_2} = -0.022\right)$ and shown in figure 19. In this figure, cold-wall Stanton numbers are plotted at each α as a function of Reynolds number and are compared with curves for laminar and turbulent heating obtained from the relations of reference 12. Stanton and Reynolds numbers were based on local conditions and Eckert's reference temperature. The calculated curves for turbulent heating followed the trend of the data for turbulent heating very well, but the data were consistently below the turbulent-heating curves by from 10 to 30 percent. This kind of agreement, as indicated in reference 13, was expected at the wall-temperature ratios of the present investigation.

Effect of stagnation temperature.- Tests 30 and 31 (table II were conducted near the lower stagnation-temperature limit of approximately 1400 K (2500° R) to observe any effects of stagnation temperature on panel heating that might arise from unknown anomalies in the test stream over the stagnation-temperature range of the facility. Center-line $\left(\frac{y}{w_2} = -0.022\right)$ cold-wall Stanton numbers obtained from these tests are compared in figure 20 with center-line Stanton numbers obtained from tests 26 and 29 which were conducted near the upper stagnation-temperature limit of approximately 1900 K (3400° R). The data shown from both test series were obtained at a stagnation pressure of approximately 17.65 MPa (2560 psia) for $\alpha = 0^{\circ}$ and 15° using the smaller boundary-layer trip diameter. The results indicate excellent correlation among the four sets of data and, therefore, no effect of stagnation temperature.

Summary of panel loading and heating results.- Variations with α of the ratio of average surface pressure to free-stream static pressure and of average cold-wall turbulent Stanton numbers based on free-stream static conditions are presented in figure 21 from tests 18 to 29 (table II). Pressure ratios from 1.05 to 9.20 were obtained between $\alpha = 0^{\circ}$ and 18°. The pressure ratio shown at $\alpha = 18^{\circ}$ was obtained from test 14 (table II) in which the panel was pitched gradually above $\alpha = 15^{\circ}$ to find the angle of attack at which flow breakdown occurred. In that test, it occurred just above 18°. Cold-wall Stanton numbers varied from 7×10^{-4} to 3×10^{-3} between $\alpha = 0^{\circ}$ and 15°. Average pressure ratios can be predicted within ±10 percent using oblique-shock relations (ref. 8), and average turbulent heating rates are overpredicted from 10 to 30 percent using Eckert's reference temperature (ref. 12).

Carpet plots summarizing the available average flat-plate surface pressures and cold-wall turbulent heating rates obtained from tests 18 to 29 (table II) are presented in figure 22 for angles of attack to 15°, for tunnel combustion-chamber pressures from 6.9 to 24.1 MPa (1000 to 2500 psia), and for a stagnation temperature of 1900 K (3400° R). In this range of test conditions, surface pressures from 0.9 to 15.2 Pa (0.13 to 2.20 psia) and cold-wall turbulent heating rates from 29.5 to 250 kW/m^2 (2.6 to 22.0 Btu/ft^2-sec) are obtained in the Langley 8-foot high-temperature structures tunnel.

Panel-Holder Configuration Development

The modified panel-holder configuration was assembled after evaluating the effects of leading-edge radius, boundary-layer trips, and aerodynamic fences separately. A discussion of these effects follows.

Effects of leading-edge bluntness on local Mach numbers.- Leading-edge bluntness markedly affected Mach number distributions in the flow field outside the boundary layer as shown by data from the pitot survey rake in figures 23 and 24 for the blunt and sharp leading edges, respectively. The data of figure 23 were from tests 2 to 10 (table II), and the data of figure 24 were from tests 11 to 14. With the blunt leading edge, Mach numbers increased with increasing height above the surface at a distance on the center line of $\frac{x}{w_1} = 1.76$ (or 134 leading-edge diameters). With the sharp leading edge, the Mach numbers were constant above the surface at a distance of $\frac{x}{w_2} = 1.85$ for all free-stream unit Reynolds numbers and α shown. Mach number variations similar to those of figure 23 were reported in reference 14 and are a leading-edge bluntness effect observed in hypersonic flow arising from large changes in entropy that occur when streamlines cross the nearly normal portions of the detached bow shock wave (refs. 15 and 16). Thus, for the first 10 tests of table II, the calibration panel was located under a flow field where bluntness effects prevailed. At $\alpha = 0°$, losses through the entropy layer reduced the Mach number nearest the surface nearly 50 percent. As α increased, the thickness of the entropy layer decreased to the extent that at $\alpha = 15°$ (fig. 23(d)) the Mach numbers obtained from the two upper probes on the survey rake were equal. The Mach number given by the probe nearest the surface appeared not to vary with α. With the sharp leading edge, the Mach numbers shown in figure 24 decreased with increasing α as expected and appeared to be the values which the Mach numbers in figure 23 were approaching with increasing distance from the surface.

The curves shown in figure 23 indicate that the Lockheed inlet program of reference 9 predicted the Mach number variation through the entropy layer very well for $\alpha > 0°$. The dashed line at the lower edge of each plot in figure 23 indicates that a fair to good approximation of the Mach number near the surface as given by the lower pitot probe was obtained, assuming isentropic expansion from the total pressure behind a normal shock

to the static pressure given by oblique-shock relations (ref. 8). These relations also predicted the Mach number in the flow field outside the entropy layer, as shown by the agreement between the dashed line on the upper edge of each plot and the Mach number given by the upper pitot probe in figure 23(d) (blunt leading edge) and between the theory and data in figure 24 (sharp leading edge).

Effects of leading-edge bluntness on surface pressures.- Pressure distributions obtained along the panel center line using only the sharp, untripped leading edge in tests 11 and 13 (table II) were similar to the center-line distributions shown in figure 16 and obtained with the sharp leading edge, small boundary-layer trips, and aerodynamic fences. Hence, use of the sharp leading edge eliminated the effects of flow expansion encountered along the panel center line with the blunt leading edge at $\alpha = 0^{\circ}$. No characteristic differences in longitudinal pressure distributions attributable to leading-edge effects were observed at higher values of α. However, spanwise pressures were affected as shown in figure 25, although the smaller width of the panel holder may also have been a contributing factor to the effects observed. In this figure, spanwise pressures normalized with respect to the center-line value are plotted along station $\frac{x}{w_2} = 1.748$ at $\alpha = 0^{\circ}$ and 10° for both leading-edge configurations and two nominal free-stream unit Reynolds numbers. Thus, at $\alpha = 0^{\circ}$, the spanwise pressure rise encountered near the trailing-edge corners of the panel with the blunt leading edge (circle symbols) was reduced by nearly one-half using the sharp leading edge (square symbols). However, at $\alpha = 10^{\circ}$, the spanwise drop in pressure from the center-line value obtained using the sharp leading edge was about 30 percent greater than was obtained using the blunt leading edge.

Effect of leading-edge bluntness on surface heating rate.- The influence of leading-edge bluntness on panel aerodynamic heating rate at $\alpha = 0^{\circ}$ and 10° is demonstrated in figure 26. In this figure, center-line cold-wall Stanton numbers obtained from tests 3 and 4 (table II) using the blunt leading edge are compared with data obtained from tests 11 and 12 (table II) using the sharp leading edge. Nominal free-stream unit Reynolds number was $R_{L,\infty} = 2.0 \times 10^6$ per meter (0.6×10^6 per foot). These results indicate higher heating rates on the surface with the sharper leading edge at both values of α. Inasmuch as the data trends and heating levels were dependent upon the type of boundary layer, the higher heating rates obviously resulted from earlier boundary-layer transition. This effect of bluntness is consistent with the literature, as in reference 4. From the data of figure 26(a), it appears that the beginning of boundary-layer transition occurred on the panel with the sharp leading edge at a Reynolds number, based on conditions at the outer edge of the boundary layer, of approximately 2.7×10^6. This value appeared to correlate favorably with published transition results obtained at the present wall-temperature ratio but at higher free-stream unit Reynolds numbers as in reference 13. Thus, it can probably be assumed that the data of figure 26(a) (sharp leading edge) were not influenced by

the 0.3-cm (0.1-in.) gap at the leading edge of the panel and that this Reynolds number is a reasonable value for the natural transition Reynolds number in the test facility.

Effect of boundary-layer trips.- Turbulent heating could not be provided throughout the range of test conditions for this investigation without using the boundary-layer trips of figure 1(d). The effectiveness of the trips is demonstrated in figure 27, where center-line cold-wall Stanton numbers obtained from the sharp leading edge with and without trips are compared at $\alpha = 0^{\circ}$ for $R_{L,\infty} = 2.0 \times 10^6$ per meter (0.6×10^6 per foot). These data show that by increasing the trip diameter the location of boundary-layer transition can be moved upstream so that heating rates can correspondingly increase from transitional to fully turbulent values. In figure 28, all center-line cold-wall heating data obtained with the sharp leading edge (without fences, tests 11 to 18 in table II) are compared with curves for the laminar and turbulent theories of reference 12. These results indicate that fully turbulent heating is achievable over the present range of test conditions by using the appropriate boundary-layer trip diameter. The range of α and unit Reynolds number over which each trip diameter is required for turbulent heating is summarized in table IV, where it is seen that boundary-layer trips are required for turbulent flow over the panel surface at angles of attack less than 10° and free-stream unit Reynolds numbers below 4.9×10^6 per meter (1.5×10^6 per foot).

Effects of aerodynamic fences on flow patterns and surface pressures.- Without aerodynamic fences, the oil-flow patterns shown in the photographs of figure 29 were observed over the test surface during tests of a 1/12-scale model of the panel holder. These patterns were obtained from tests conducted in hot flow in the 7-inch Mach 7 pilot tunnel at the Langley Research Center and indicate that the flow streamlines turned inward from the side edges at $\alpha = 0^{\circ}$ as in figure 29(a) and outward at $\alpha = 10^{\circ}$ as in figure 29(b). Correspondingly, surface pressures were higher in areas of inflow at $\alpha = 0^{\circ}$ and decreased in areas of outflow at $\alpha > 0^{\circ}$, as was illustrated in the pictorial representations of figure 9. Use of the aerodynamic-fence configuration of figure 1 greatly diminished this α-dependent tendency of the flow streamlines to deflect, as shown by the oil-flow patterns of figure 30 for $\alpha = 0^{\circ}$ and 10°. (This effect is well-documented as, for example, in ref. 12.)

Accordingly, the use of aerodynamic fences also diminished the corresponding α-dependent variations in surface pressures near the trailing-edge corners except at $\alpha = 0^{\circ}$ and $R_{L,\infty} = 2.0 \times 10^6$ per meter (0.6×10^6 per foot) as shown in figure 31. In this figure, pressures obtained along station $\frac{x}{w_2} = 1.748$ on the panel holder with the sharp leading edge without fences are compared with pressures obtained from the modified panel holder (sharp, tripped leading edge with fences) at $\alpha = 0^{\circ}$ and 15° for two free-stream unit Reynolds numbers. The pressures were normalized with respect to the center-line value. Except for the conditions shown in figure 31(a), the spanwise

change in pressure near the trailing-edge corners was reduced as much as 50 percent with fences attached. The spanwise change in pressure with fences attached was about 2 percent at $\alpha = 0^{\circ}$ (fig. 31(b)) and was about 12 percent at $\alpha = 10^{\circ}$ and 15°.

CONCLUSIONS

Surface pressure and heating-rate distributions (wall-temperature to total-temperature ratio approximately 0.2) were obtained on a large, flat calibration panel at a nominal Mach number of 7 in the Langley 8-foot high-temperature structures tunnel. Panel dimensions were 108.0 by 152.4 cm (42.5 by 60.0 in.). Test objectives were (1) to map available flat-plate loading and heating and (2) to determine the effectiveness of leading-edge bluntness, boundary-layer trips, and aerodynamic fences in generating a uniform, streamwise turbulent flow field over the test surface. Tests were conducted at angles of attack to 15° for free-stream unit Reynolds numbers from 1.240×10^6 to 5.545×10^6 per meter (0.378×10^6 to 1.69×10^6 per foot). Stagnation pressures were from 4.275 to 18.06 MPa (620 to 2620 psia); stagnation temperatures were 1400 K (2500° R) and 1900 K (3400° R). The following conclusions are indicated:

1. Surface pressures from 0.90 to 15.2 kPa (0.13 to 2.20 psia) and cold-wall turbulent heating rates from 29.5 to 250 kW/m^2 (2.6 to 22.0 Btu/ft^2-sec) are available in the present range of test conditions.

2. Average pressures can be predicted within ±10 percent using oblique-shock relations, and average turbulent heating rates are overpredicted from 10 to 30 percent using Eckert's reference temperature, as was expected for the present wall-temperature to total-temperature ratio.

3. For a free-stream unit Reynolds number of 2.0×10^6 per meter (0.6×10^6 per foot), the local Reynolds number for natural boundary-layer transition in the Langley 8-foot high-temperature structures tunnel is approximately 2.7×10^6.

4. A sharp leading edge produces a flow field above the panel surface in which the Mach number is constant, whereas a blunt leading edge generates an entropy gradient that reduces the Mach number near the surface by almost 50 percent at $\alpha = 0^{\circ}$.

5. Boundary-layer trips are required for turbulent flow over the panel surface at angles of attack less than 10° and free-stream unit Reynolds numbers below 4.9×10^6 per meter (1.5×10^6 per foot).

6. Aerodynamic fences diminish the tendency of flow streamlines to deflect with angle of attack and reduce spanwise surface pressure variations near the trailing edge as much as 50 percent.

7. With a sharp leading edge, boundary-layer trips, and aerodynamic fences attached to the panel holder, pressures along the panel center line vary within ±5 percent. The spanwise change in pressure near the trailing edge of the panel is about 2 percent at an angle of attack of 0^{o} for free-stream unit Reynolds number of 4.9×10^{6} per meter (1.5×10^{6} per foot) and about 12 percent at angles of attack of 10^{o} and 15^{o}. Turbulent heating rates decrease longitudinally by about 15 percent and vary within ±5 percent in the spanwise direction.

Langley Research Center,
National Aeronautics and Space Administration,
Hampton, Va., May 22, 1973.

APPENDIX

CONVERSION OF U.S. CUSTOMARY UNITS TO SI UNITS

Factors required for converting U.S. Customary Units to the International System of Units (SI) are given in the following table:

Physical quantity	U.S. Customary Unit	Conversion factor (*)	SI Unit
Heat flux	Btu/ft^2-sec	11348.9	watt/meter^2 (W/m^2)
Length	in.	0.0254	meter (m)
	ft	0.3048	meter (m)
	per ft	3.28083	per meter (m^{-1})
Pressure	psi	6894.757	pascal (Pa)
Temperature	^oR	5/9	kelvin (K)

*Multiply value in U.S. Customary Unit by conversion factor to obtain equivalent value in SI Unit.

Prefixes to indicate multiples of units are as follows:

Prefix	Multiple
mega (M)	10^6
kilo (k)	10^3
centi (c)	10^{-2}
milli (m)	10^{-3}
micro (μ)	10^{-6}

REFERENCES

1. Anderson, Roger A.; Brooks, William A., Jr.; Leonard, Robert W.; and Maltz, Joseph: Structures – A Technology Overview. Astronaut. & Aeronaut., vol. 9, no. 2, Feb. 1971, pp. 38-47.

2. Weinstein, Irving: Heat-Transfer and Pressure Distributions on Hemisphere-Cylinders in Methane-Air Combustion Products at Mach 7. NASA TN D-7104, 1973.

3. Comm. on Metric Pract.: ASTM Metric Practice Guide. NBS Handbook 102, U.S. Dep. Com., Mar. 10, 1967.

4. Holloway, Paul F.; and Morrisette, E. Leon: Roughness Effects on Boundary-Layer Transition for Blunt-Leading-Edge Plates at Mach 6. NASA TN D-3517, 1966.

5. Sterrett, James R.; Morrisette, E. Leon; Whitehead, Allen H., Jr.; and Hicks, Raymond M.: Transition Fixing for Hypersonic Flow. NASA TN D-4129, 1967.

6. Stone, David R.; and Cary, Aubrey M., Jr.: Discrete Sonic Jets Used as Boundary-Layer Trips at Mach Numbers of 6 and 8.5. NASA TN D-6802, 1972.

7. Leyhe, E. W.; and Howell, R. R.: Calculation Procedure for Thermodynamic, Transport, and Flow Properties of the Combustion Products of a Hydrocarbon Fuel Mixture Burned in Air With Results for Ethylene-Air and Methane-Air Mixtures. NASA TN D-914, 1962.

8. Ames Research Staff: Equations, Tables, and Charts for Compressible Flow. NACA TR 1135, 1953. (Supersedes NACA TN 1428.)

9. Maslowe, S. A.; and Benson, J. L.: Computer Program for the Design and Analysis of Hypersonic Inlets. Rep. No. 18079 (Contract NAS 2-1460), Lockheed-California Co., Aug. 10, 1964. (Available as NASA CR-77749.)

10. Garrett, L. Bernard; and Pitts, Joan I.: A General Transient Heat-Transfer Computer Program for Thermally Thick Walls. NASA TM X-2058, 1970.

11. Eckert, Ernst R. G.: Survey on Heat Transfer at High Speeds. ARL 189, U.S. Air Force, Dec. 1961. (Available from DDC as AD 274109.)

12. Kays, W. M.: Convective Heat and Mass Transfer. McGraw-Hill Book Co., Inc., c.1966.

13. Cary, Aubrey M., Jr.: Turbulent Boundary-Layer Heat-Transfer and Transition Measurements With Surface Cooling at Mach 6. NASA TN D-5863, 1970.

14. Stone, Howard W.: The Leading-Edge Effects on the Laminar Flat-Plate Boundary Layer and the Aerodynamic Heating at Mach 10.4. NASA TN D-5160, 1969.

15. Neal, Luther, Jr.: A Study of the Pressure, Heat Transfer, and Skin Friction on Sharp and Blunt Flat Plates at Mach 6.8. NASA TN D-3312, 1966.

16. Cox, R. N.; and Crabtree, L. F.: Elements of Hypersonic Aerodynamics. Academic Press, Inc., 1965.

TABLE I.- LOCATION OF INSTRUMENTATION OF CALIBRATION PANEL

Pressure orifices				Thermocouples							
x		y		x		y		x		y	
cm	in.	cm	in.	cm	in.	cm	in.	cm	in.	cm	in.
107.0	42.1	0	0	110.8	43.6	-52.3	-20.6	185.0	72.8	-52.3	-20.6
↓	↓	15.8	6.2	↓	↓	-35.8	-14.1	↓	↓	-3.0	-1.2
↓	↓	32.5	12.8	↓	↓	-19.8	7.8	↓	↓	19.0	7.5
↓	↓	48.8	19.2	↓	↓	-3.0	-1.2	↓	↓	35.6	14.0
118.8	46.8	0	0	↓	↓	19.0	7.5	↓	↓	52.0	20.5
131.6	51.8	↓	↓	↓	↓	35.6	14.0	197.7	77.8	-3.0	-1.2
144.3	56.8	↓	↓	↓	↓	51.3	20.2	197.7	77.8	35.6	14.0
157.0	61.8	↓	↓	121.4	47.8	-3.0	-1.2	210.2	82.8	-52.3	-20.6
↓	↓	15.8	6.2	121.4	47.8	35.6	14.0	↓	↓	-35.8	-14.1
↓	↓	32.5	12.8	134.0	52.8	-52.3	-20.6	↓	↓	-19.8	-7.6
↓	↓	48.8	19.2	↓	↓	-3.0	-1.2	↓	↓	-3.0	-1.2
169.7	66.8	0	0	↓	↓	19.0	7.5	↓	↓	19.0	7.5
182.3	71.8	↓	↓	↓	↓	35.6	14.0	↓	↓	35.6	14.0
195.1	76.8	↓	↓	↓	↓	51.3	20.2	↓	↓	52.0	20.5
208.0	81.8	-48.8	-19.2	146.9	57.8	-3.0	-1.2	223.0	87.8	-3.0	-1.2
↓	↓	-32.5	-12.8	146.9	57.8	35.6	14.0	223.0	87.8	35.6	14.0
↓	↓	-15.0	-6.2	159.5	62.8	-51.3	-20.6	236.0	92.8	-52.3	-20.6
↓	↓	0	0	↓	↓	-35.8	-14.1	↓	↓	19.0	7.5
↓	↓	15.8	6.2	↓	↓	-19.8	-7.6	↓	↓	35.6	14.0
↓	↓	32.5	12.8	↓	↓	-3.0	-1.2	↓	↓	52.0	20.5
↓	↓	48.8	19.2	↓	↓	19.0	7.5	248.5	97.8	-52.3	-20.6
220.4	86.8	0	0	↓	↓	35.6	14.0	↓	↓	-35.8	-14.1
233.5	91.8	↓	↓	↓	↓	52.0	20.5	↓	↓	-19.8	-7.6
246.0	96.8	↓	↓	172.2	67.8	-3.0	-1.2	↓	↓	-3.0	-1.2
↓	↓	15.8	6.2	172.2	67.8	35.6	14.0	↓	↓	19.0	7.5
↓	↓	32.5	12.8					↓	↓	35.6	14.0
↓	↓	48.8	19.2					↓	↓	52.0	20.5

TABLE II.- TEST CONDITIONS AND PANEL-HOLDER CONFIGURATIONS

Test	T_t		p_t		p'_t		p_∞		$R_{L,\infty}$		$(\rho V c_p)_\infty$		M_∞	α, deg	Leading edge	Fence	Trip diameter	
	K	^oR	MPa	psia	kPa	psia	kPa	psia	per meter	per foot	kW/m^2-K	Btu/ft^2-sec-^oR					cm	in.
1	1944	3500	4.275	620	33.10	4.80	0.5295	0.0768	1.240×10^6	0.378×10^6	18.11	0.886	6.94	-0.3	Blunt	Without	0	0
2	1889	3400	4.378	635	32.96	4.78	.5275	.0765	1.322	.403	18.62	.911	6.94	10.0				
3	1917	3450	6.792	985	53.44	7.75	.8688	.126	2.037	.621	29.84	1.46	6.88	-.6				
4	1867	3360	7.033	1020	53.44	7.75	.8688	.126	2.142	.653	30.25	1.48	6.88	10.0				
5	1944	3500	6.895	1000	52.68	7.64	.8550	.124	1.988	.606	29.02	1.42	6.88	15.0				
6	1911	3440	12.14	1760	95.15	13.8	1.607	.233	3.642	1.11	53.35	2.61	6.75	-.6				
7	1928	3470	12.27	1780	93.77	13.6	1.586	.230	3.445	1.05	52.12	2.55	6.75	4.5				
8	1967	3540	12.34	1790	96.53	14.0	1.638	.231	3.510	1.07	52.94	2.59	6.75	10.0				
9	1822	3280	17.72	2570	135.8	19.7	2.379	.345	5.413	1.65	78.90	3.86	6.64	-.6				
10	1906	3430	17.65	2560	132.4	19.2	2.317	.336	4.954	1.51	74.81	3.66	6.64	4.5				
11	1778	3200	7.033	1020	48.70	6.99	.7929	.115	2.044	.623	30.87	1.51	6.74	0	Sharp			
12	1900	3420	7.033	1020	47.78	6.93	.7378	.107	1.821	.555	26.37	1.29	7.00	10.0				
13	1533	2760	17.72	2570	111.7	16.2	2.193	.318	5.118	1.56	69.50	3.40	6.13	0				
14	1633	2940	17.86	2590	118.6	17.2	2.234	.324	5.315	1.62	71.34	3.49	6.31	9.9				
15	1856	3340	7.171	1040	49.02	7.11	.7791	.113	1.952	.595	27.39	1.34	6.90	0			.24	.094
16	1850	3330	17.93	2600	122.7	17.8	2.117	.307	4.823	1.47	69.09	3.38	6.60	0				
17	1828	3290	17.86	2590	122.7	17.8	2.110	.306	4.921	1.50	69.91	3.42	6.68	15.0				
18	1900	3420	6.964	1010	47.58	6.90	.7447	.108	1.854	.565	26.16	1.28	6.98	0			.48	.19
19	1828	3290	7.033	1020	48.40	7.02	.7722	.112	1.972	.601	27.19	1.33	6.88	0		Attached	.24	.094
20	1917	3450	7.033	1020	47.78	6.93	.7378	.107	1.755	.535	26.16	1.28	6.99	5.0				
21	1722	3100	7.033	1020	48.20	6.99	.8136	.118	2.110	.643	28.41	1.39	6.76	9.9				
22	1750	3150	7.033	1020	48.26	7.00	.7998	.116	2.080	.634	28.21	1.38	6.79	14.9				
23	1911	3440	12.34	1790	84.12	12.2	1.365	.198	3.035	.925	44.97	2.20	6.81	0				
24	1911	3440	12.34	1790	84.12	12.2	1.365	.198	3.314	1.01	47.02	2.30	6.81	9.9				
25	1867	3360	12.34	1790	84.12	12.2	1.393	.202	3.314	1.01	47.02	2.30	6.82	14.9				
26	1867	3360	18.06	2620	124.1	18.0	2.117	.307	4.757	1.45	68.89	3.37	6.64	0				
27	1839	3310	17.65	2560	121.4	17.6	2.089	.303	4.823	1.47	68.89	3.37	6.69	4.8				
28	1817	3270	17.79	2580	122.7	17.8	2.144	.311	4.888	1.49	69.91	3.42	6.60	9.8				
29	1789	3220	17.65	2560	121.4	17.6	2.137	.310	4.888	1.49	69.71	3.41	6.55	15.1				
30	1411	2540	17.65	2560	102.0	14.8	2.117	.307	5.249	1.60	68.68	3.36	5.99	0				
31	1444	2600	17.65	2560	105.5	15.3	2.151	.312	5.545	1.69	70.73	3.46	6.10	15.0				

TABLE III.- LOCAL TEST CONDITIONS AND CONVERSION FACTORS

Test	T_l		p_l		T_{aw}		T^*		$\frac{R_{L,l}}{R_{L,\infty}}$	$\frac{(\rho V c_p)_l}{(\rho V c_p)_\infty}$	$\frac{R^*_{L,l}}{R_{L,\infty}}$	$\frac{(\rho V c_p)^*_l}{(\rho V c_p)_\infty}$
	K	°R	kPa	psia	K	°R	K	°R				
1	577.8	1040	0.5295	0.0768	1722	3100	744.4	1340	0.147	0.313	0.0822	0.237
2	877.8	1580	2.289	.332	1689	3040	788.9	1420	.247	.824	.294	.906
3	555.6	1000	.8688	.126	1700	3060	716.7	1290	.153	.321	.0821	.218
4	866.7	1560	3.723	.540	1672	3010	777.8	1400	.253	.830	.296	.907
5	1044	1880	6.316	.916	1756	3160	850.0	1530	.320	1.19	.434	1.35
6	555.6	1000	1.606	.233	1694	3050	711.1	1280	.158	.332	.0827	.220
7	716.7	1290	3.234	.469	1717	3090	750.0	1350	.205	.537	.174	.484
8	905.6	1630	6.785	.984	1761	3170	805.6	1450	.271	.853	.314	.914
9	519.4	935	2.379	.345	1611	2900	688.9	1240	.178	.348	.0761	.200
10	711.1	1280	4.654	.675	1694	3050	744.4	1340	.208	.538	.175	.487
11	211.1	380	.7929	.115	1639	2950	577.0	1040	1.00	1.00	.165	.336
12	348.9	628	3.144	.456	1761	3170	750.0	1350	1.78	2.59	.469	1.35
13	205.6	370	2.193	.318	1428	2570	416.7	950	1.00	1.00	.188	.407
14	312.2	562	8.550	1.74	1450	2610	561.1	1010	1.75	2.54	.627	1.41
15	213.3	384	.7791	.113	1711	3080	594.4	1070	1.00	1.00	.146	.345
16	228.9	412	2.117	.307	1706	3070	594.4	1070	1.00	1.00	.177	.409
17	484.4	872	15.10	2.19	1711	3080	666.7	1200	1.58	3.06	.913	2.39
18	215.0	387	.7447	.108	1756	3160	600.0	1080	1.00	1.00	.163	.385
19	210.0	378	.7722	.112	1689	3040	583.3	1050	1.00	1.00	.164	.386
20	274.4	494	1.682	.244	1778	3200	622.2	1120	1.57	1.76	.363	.834
21	327.8	590	3.330	.483	1606	2890	600.0	1080	1.70	2.57	.603	1.46
22	446.7	804	5.744	.833	1639	2950	638.9	1150	1.67	3.19	.898	2.31
23	229.4	413	1.365	.198	1767	3180	605.6	1090	1.00	1.00	.179	.407
24	355.6	640	5.716	.829	1772	3190	644.4	1160	1.69	2.59	.594	1.48
25	476.7	858	9.791	1.42	1750	3150	672.2	1210	1.66	3.16	.918	2.40
26	228.3	411	2.117	.307	1728	3110	600.0	1080	1.00	1.00	.180	.413
27	271.7	489	4.447	.645	1700	3060	605.6	1090	1.49	1.74	.356	.839
28	363.3	654	8.412	1.22	1689	3040	627.8	1130	1.61	2.44	.611	1.46
29	505.0	909	14.96	2.17	1678	3020	666.7	1200	1.50	2.96	.922	2.41
30	194.4	350	2.117	.307	1306	2350	497.2	895	1.00	1.00	.188	.406
31	418.9	754	13.44	1.95	1356	2440	572.2	1030	1.44	2.75	.835	2.02

TABLE IV.- EFFECT OF BOUNDARY-LAYER TRIP DIAMETER

Trip diameter		R_L		p_t		Type of flow			
cm	in.	per meter	per foot	MPa	psia	$\alpha = 0^o$	$\alpha = 5^o$	$\alpha = 10^o$	$\alpha = 15^o$
0	0	2.0×10^6	0.6×10^6	6.9	1000	Transitional		Transitional	
		3.3	1.0	12.1	1750	Transitional			
		4.9	1.5	17.2	2500	Transitional		Turbulent	
0.24	0.094	2.0×10^6	0.6×10^6	6.9	1000	Transitional	Turbulent	Turbulent	Turbulent
		3.3	1.0	12.1	1750	Transitional		Turbulent	Turbulent
		4.9	1.5	17.2	2500	Turbulent	Turbulent	Turbulent	Turbulent
0.47	0.19	2.0×10^6	0.6×10^6	6.9	1000	Turbulent			

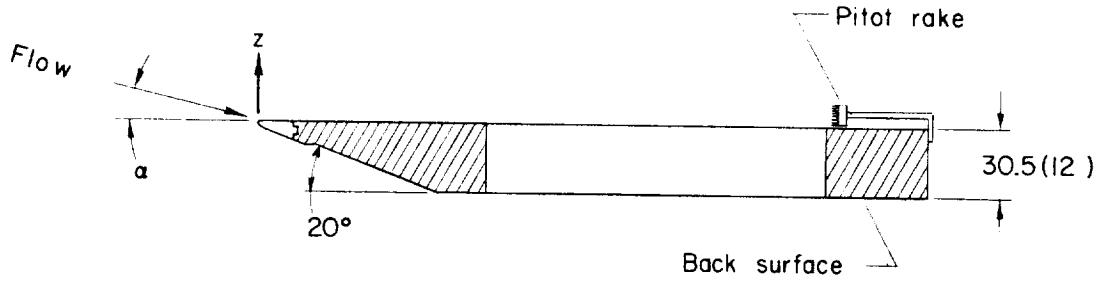

(a) Longitudinal cross section.

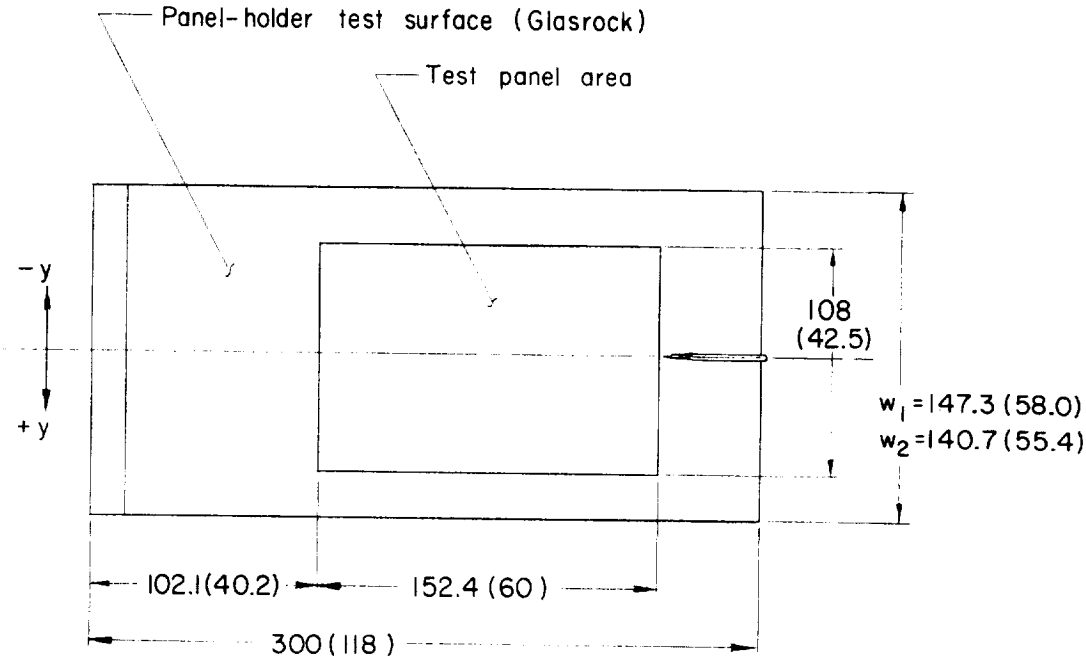

(b) Planview.

Figure 1.- Details of panel holder. All dimensions are in cm (in.).

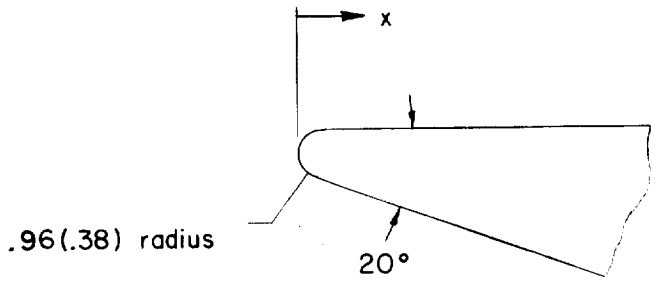

(c) Blunt leading edge.

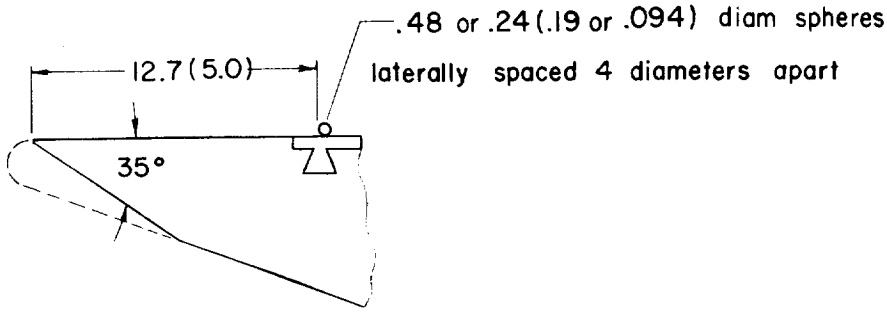

(d) Sharp leading edge and boundary-layer trips.

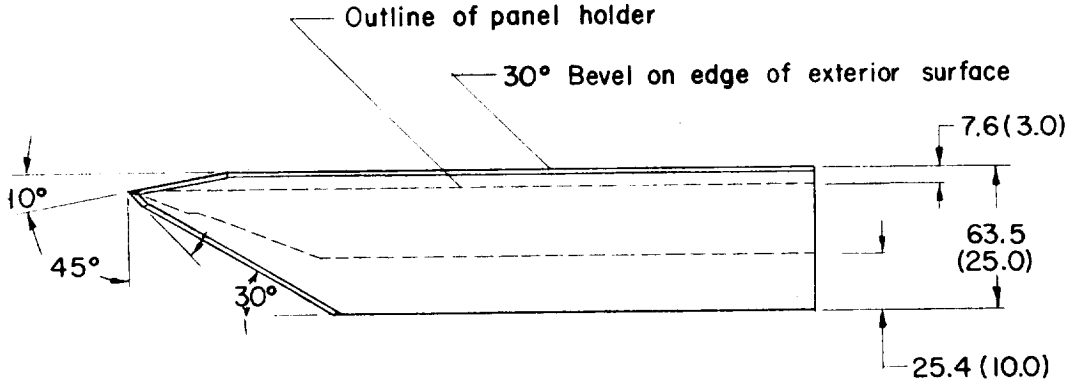

(e) Side view of aerodynamic fences.

Figure 1.- Concluded.

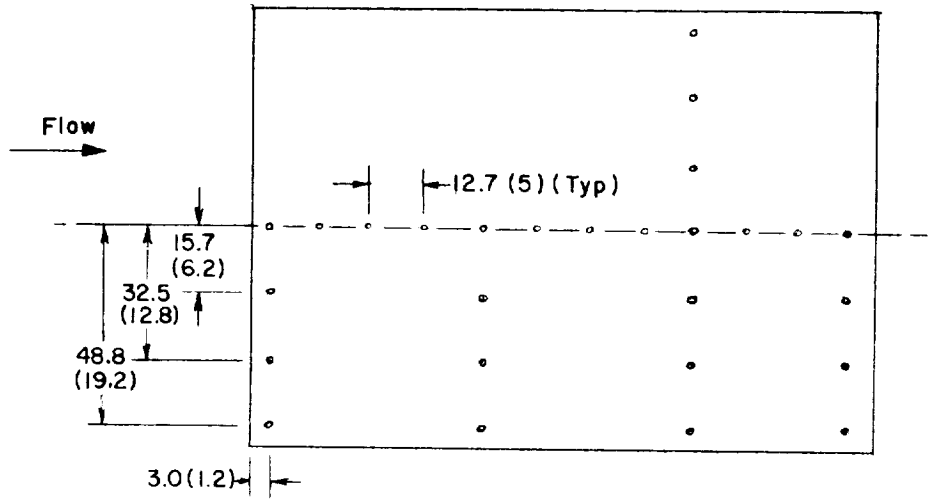

(a) Orifice distribution.

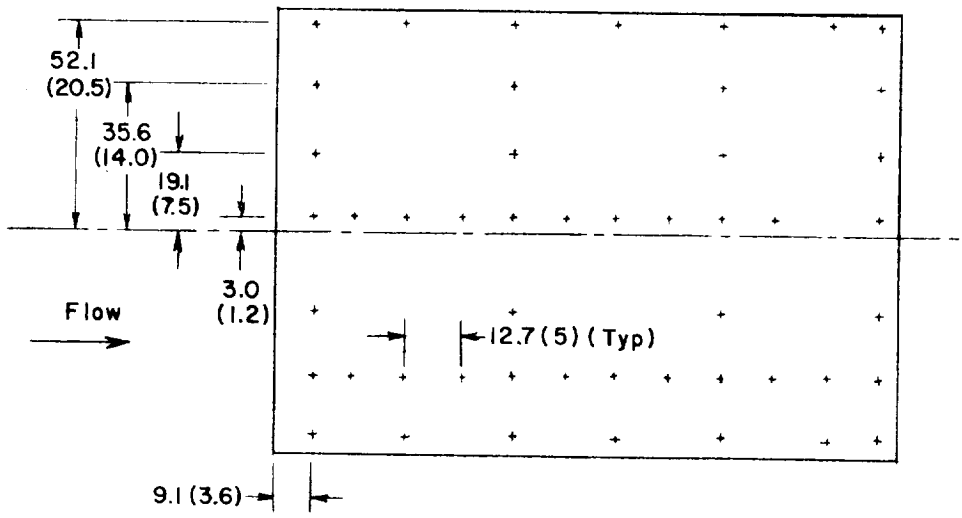

(b) Thermocouple distribution.

Figure 2.- Planview of orifice and thermocouple distributions on calibration panel. All dimensions are in cm (in.).

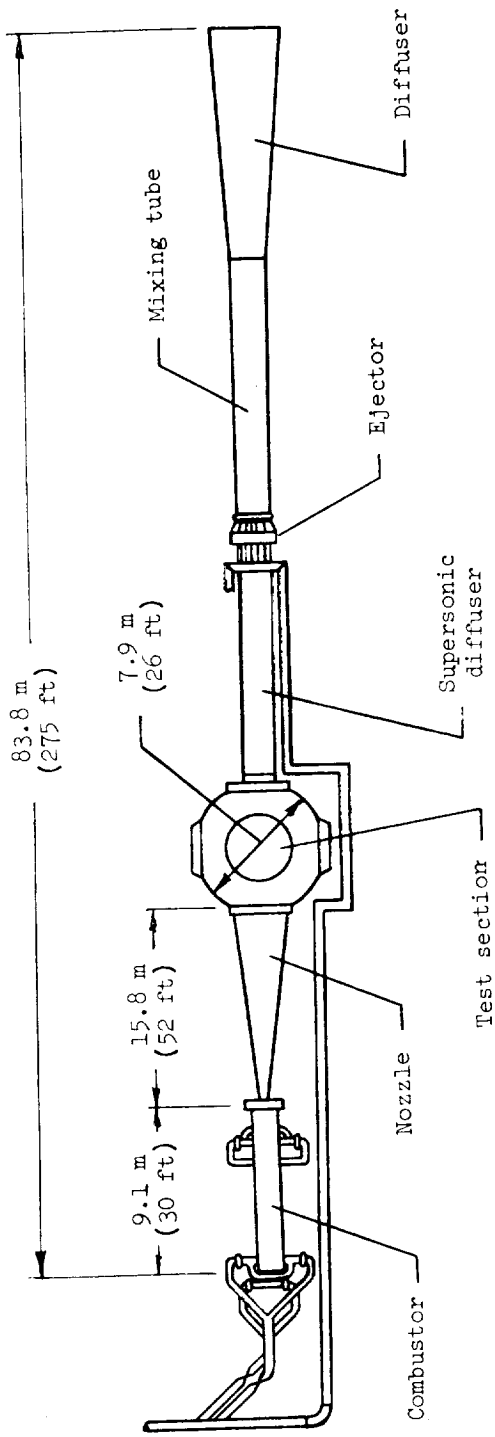

Figure 3.- Schematic of Langley 8-foot high-temperature structures tunnel.

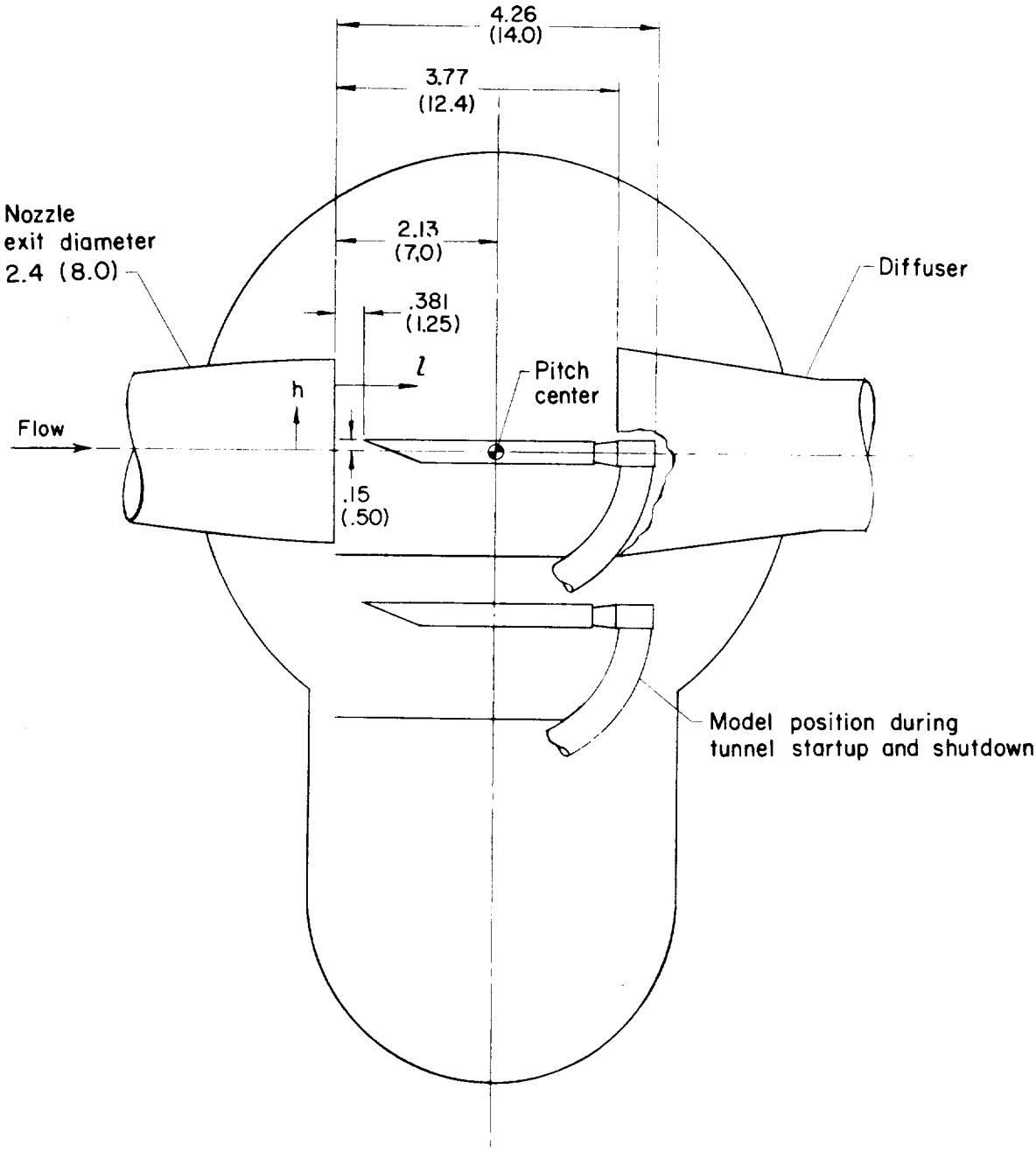

Figure 4.- Cross-sectional view of test section of the Langley 8-foot high-temperature structures tunnel. All dimensions are in m (ft).

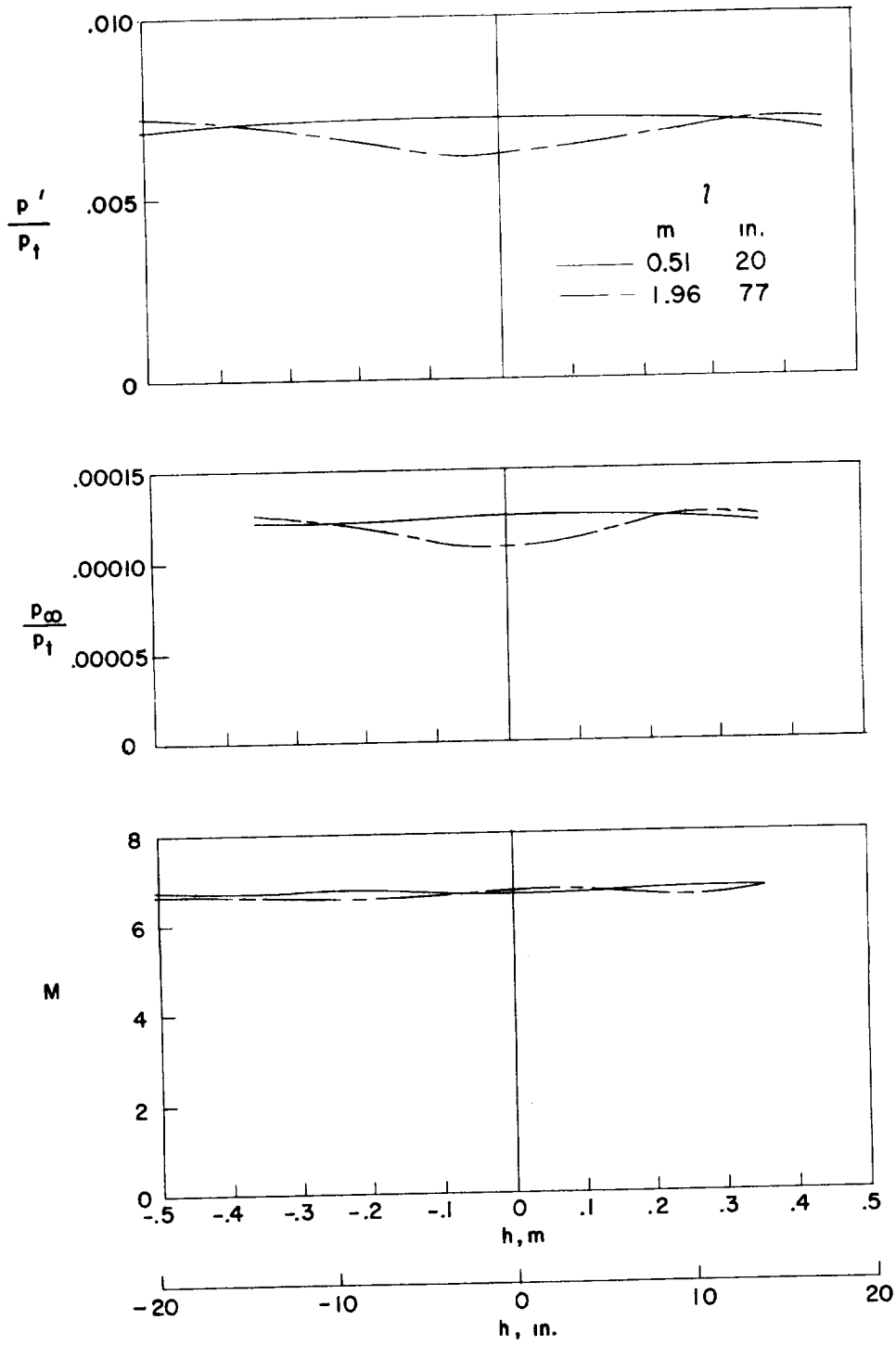

Figure 5.- Pitot pressure, static pressure, and Mach number distributions across test stream of the Langley 8-foot high-temperature structures tunnel at two longitudinal locations.

L-70-516

Figure 6.- Photograph of panel holder with blunt leading edge in the Langley 8-foot high-temperature structures tunnel.

L-71-8964

Figure 7.- Photograph of panel holder with sharp leading edge and aerodynamic fences in the Langley 8-foot high-temperature structures tunnel (modified panel-holder configuration).

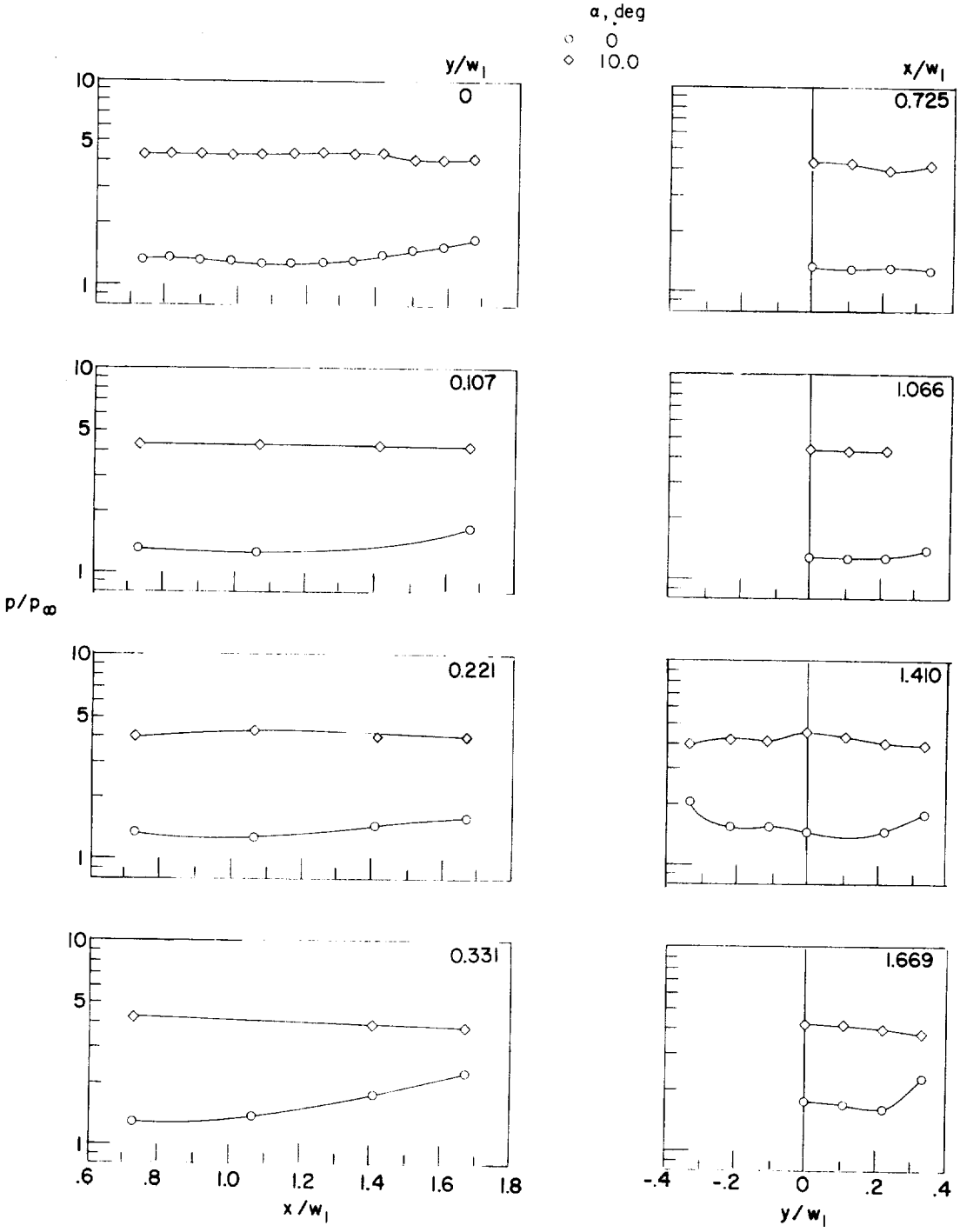

(a) $R_{L,\infty} = 1.3 \times 10^6$ per meter (0.4×10^6 per foot).

Figure 8.- Longitudinal and spanwise pressure distributions on a flat panel with a blunt leading edge and without aerodynamic fences at $M_\infty = 7$.

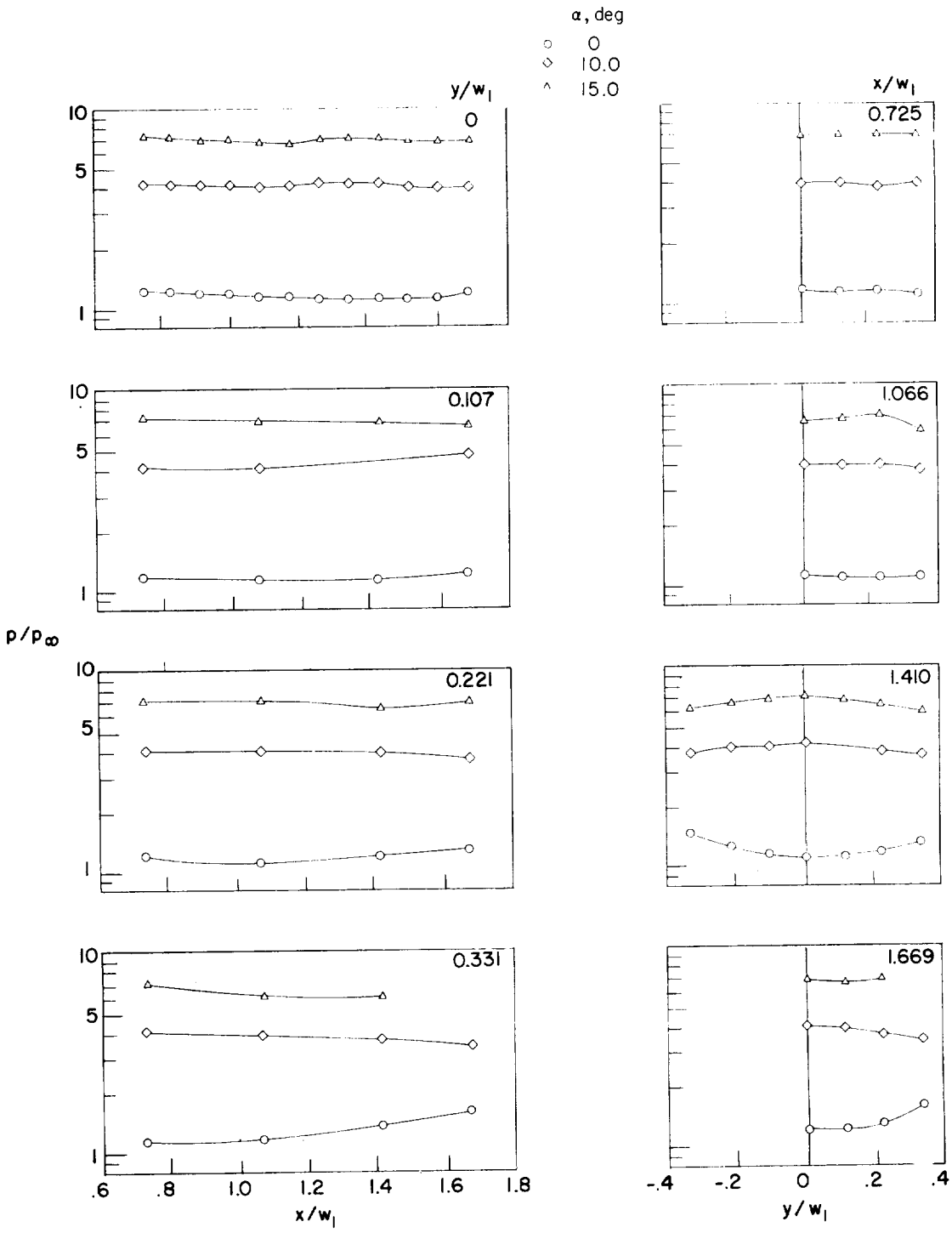

(b) $R_{L,\infty} = 2.0 \times 10^6$ per meter (0.6×10^6 per foot).

Figure 8.- Continued.

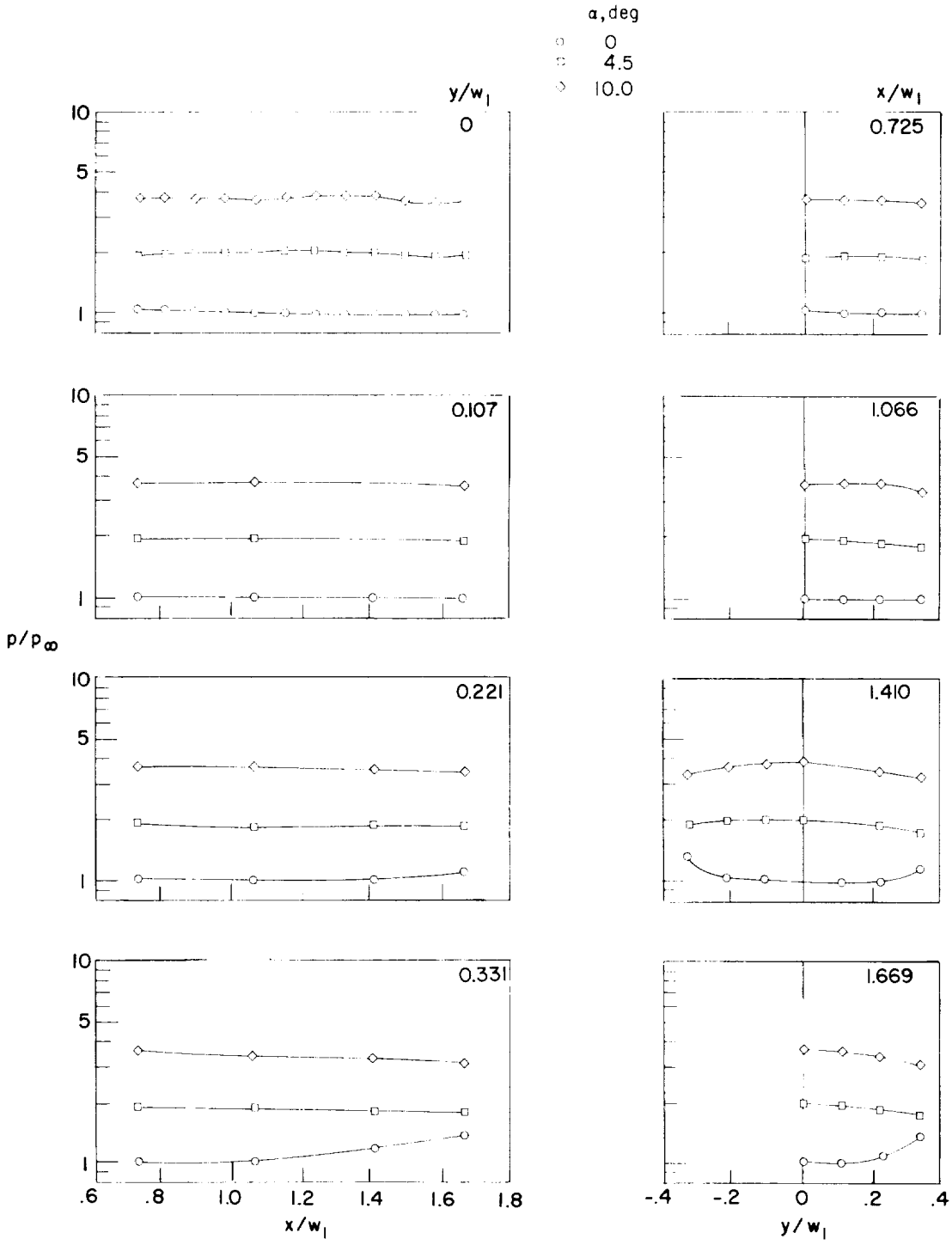

(c) $R_{L,\infty} = 3.3 \times 10^6$ per meter (1.0×10^6 per foot).

Figure 8.- Continued.

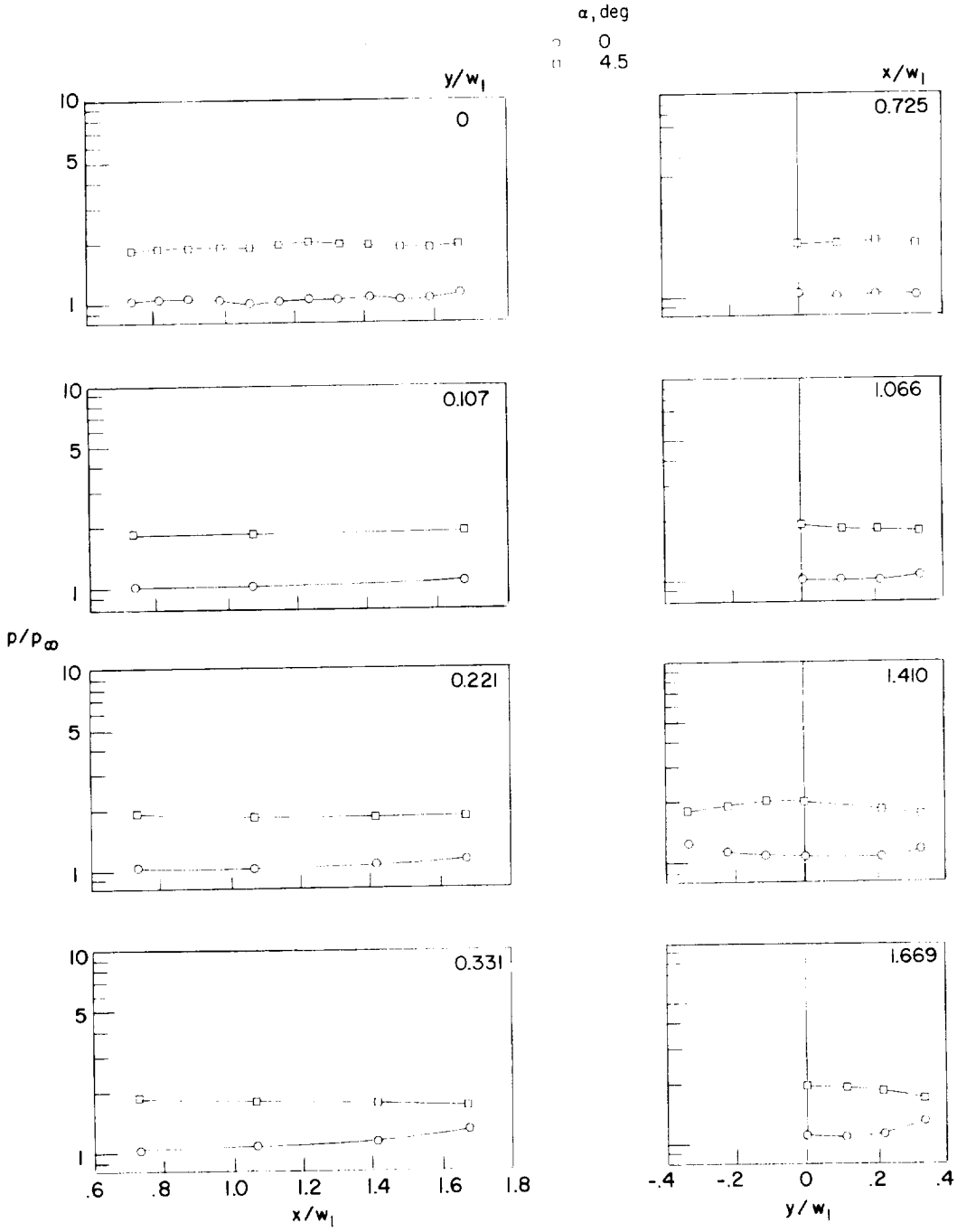

(d) $R_{L,\infty} = 4.9 \times 10^6$ per meter $(1.5 \times 10^6$ per foot).

Figure 8.- Concluded.

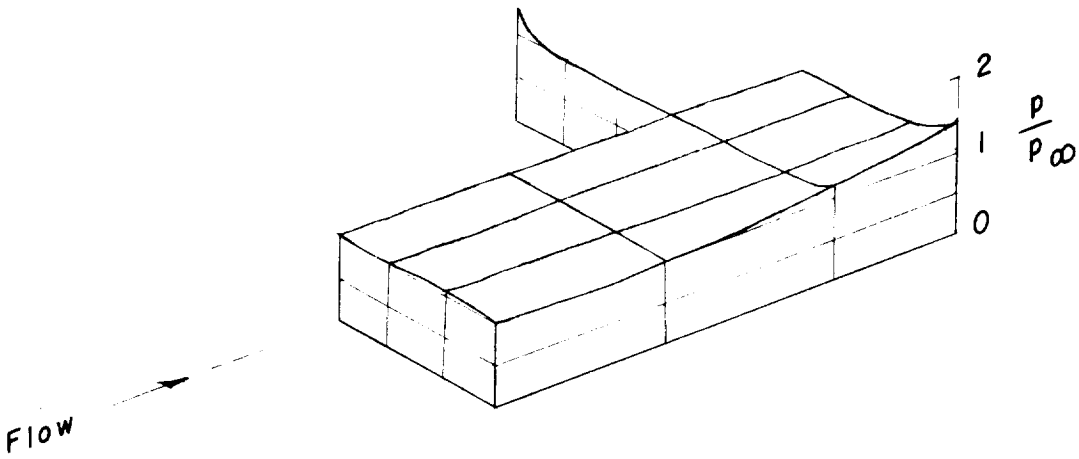

(a) $\alpha = 0^{o}$.

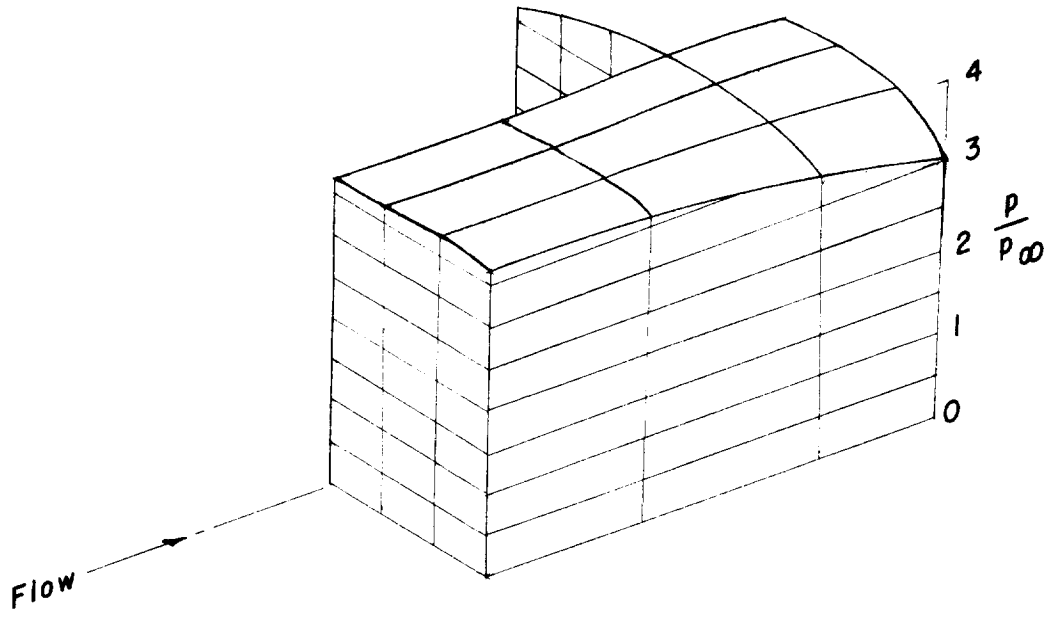

(b) $\alpha = 10^{o}$.

Figure 9.- Pressure distribution on a flat panel with a blunt leading edge and without aerodynamic fences at $R_{L,\infty} = 3.3 \times 10^{6}$ per meter (1.0×10^{6} per foot) and $M_{\infty} = 7$.

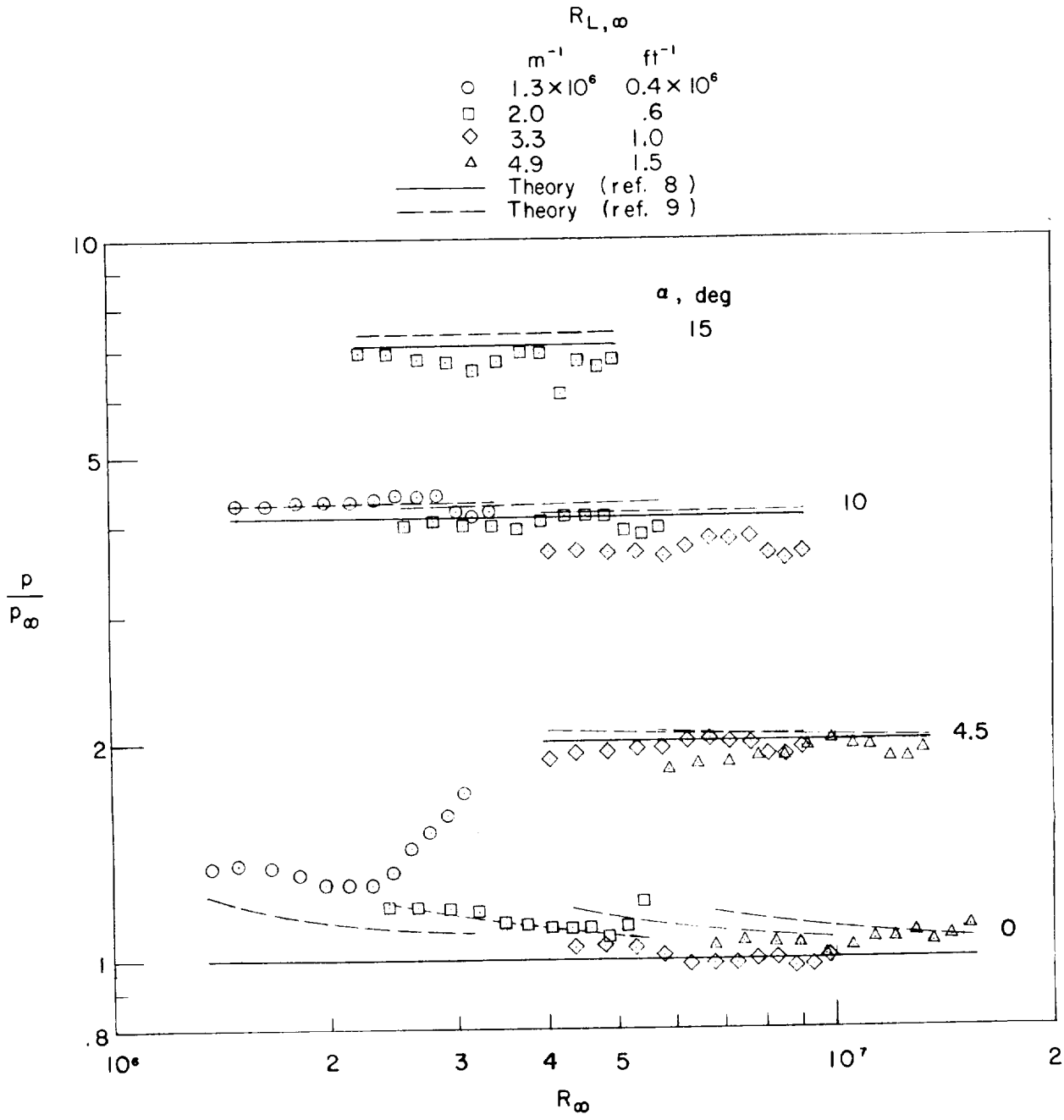

Figure 10.- Center-line pressure distributions along flat panel with blunt leading edge at $M_\infty = 7$.

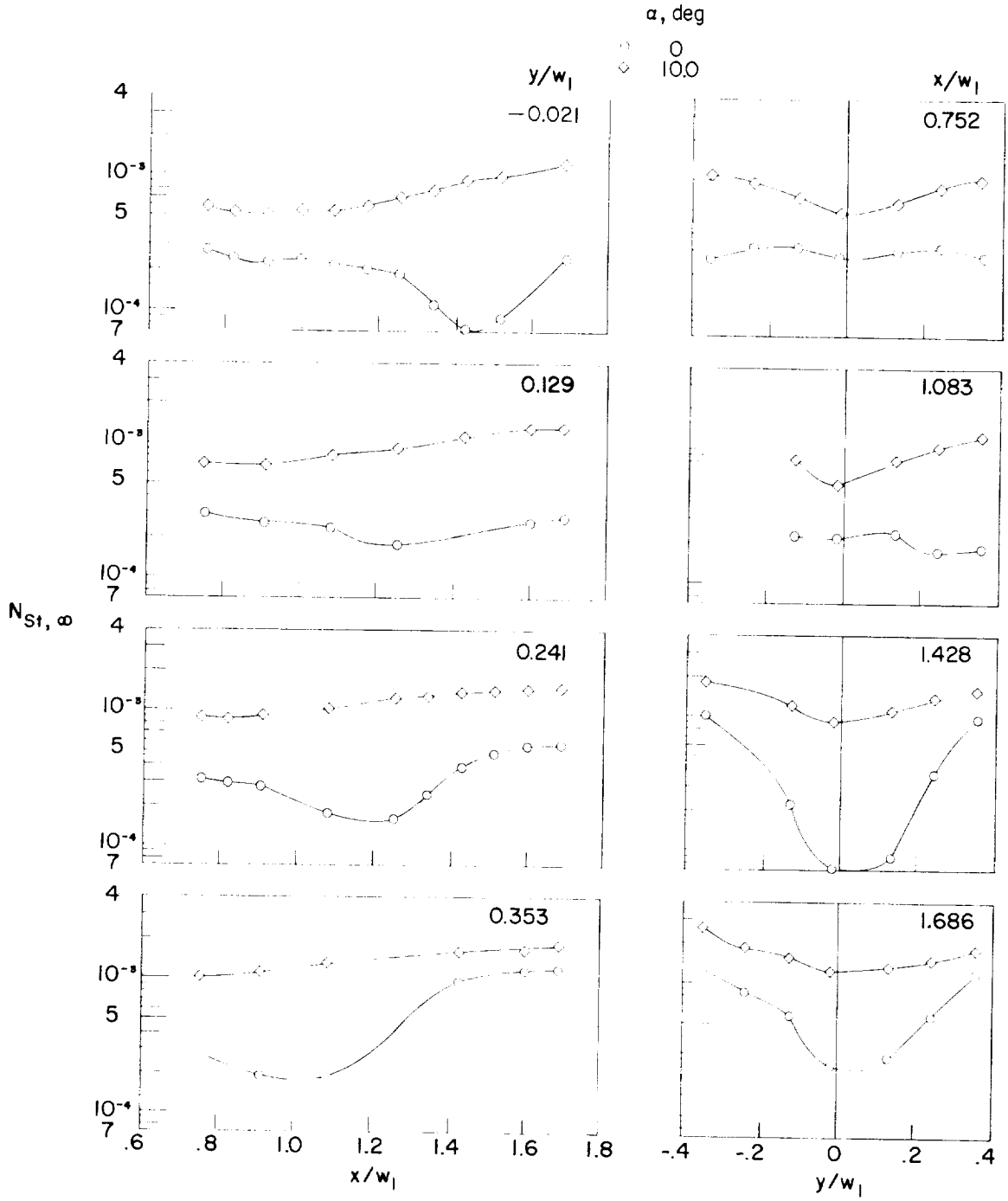

(a) $R_{L,\infty} = 1.3 \times 10^6$ per meter (0.4×10^6 per foot).

Figure 11.- Longitudinal and spanwise cold-wall heat-transfer distributions on flat panel with blunt leading edge and without aerodynamic fences at $M_\infty = 7$.

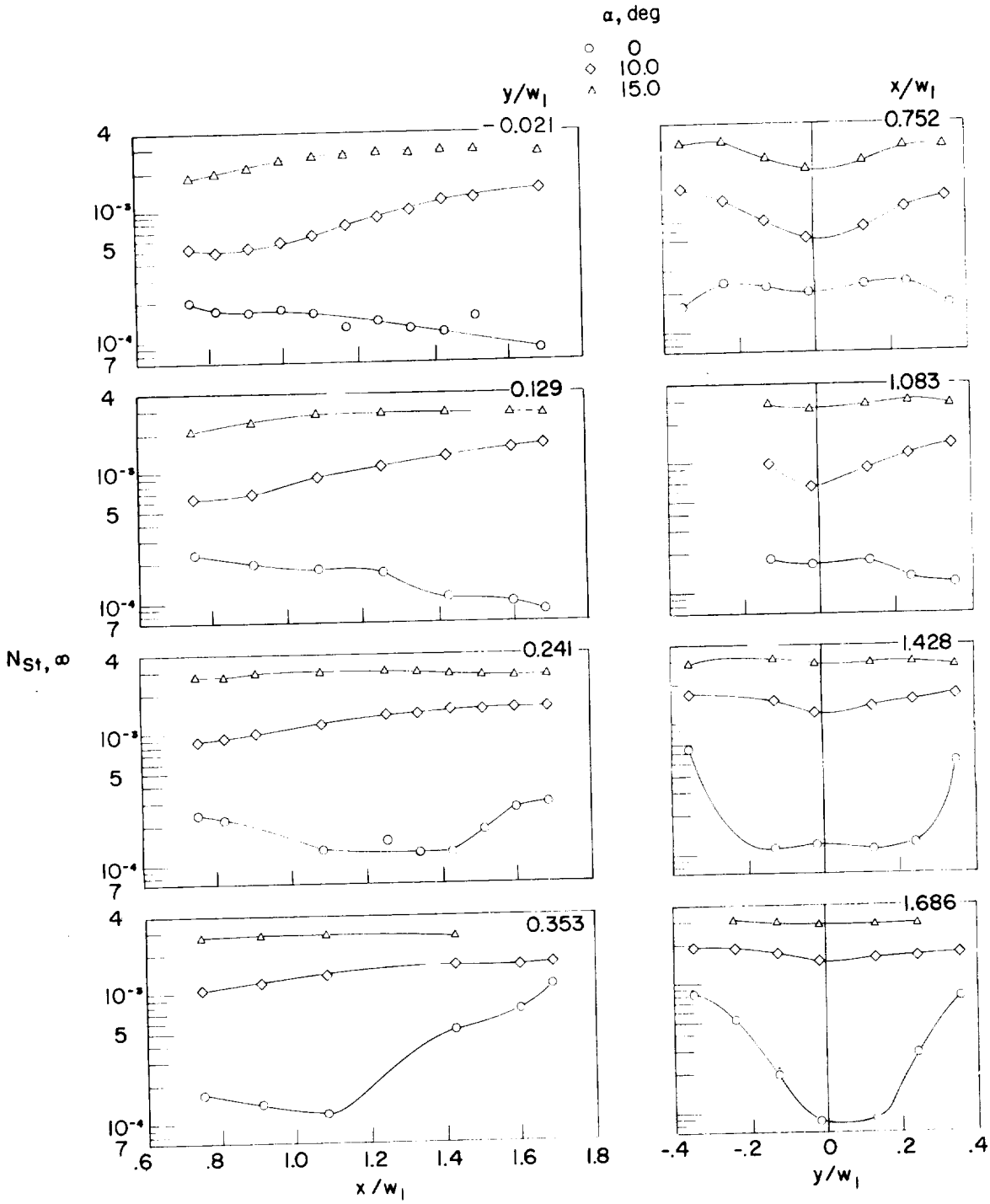

(b) $R_{L,\infty} = 2.0 \times 10^6$ per meter (0.6×10^6 per foot).

Figure 11.- Continued.

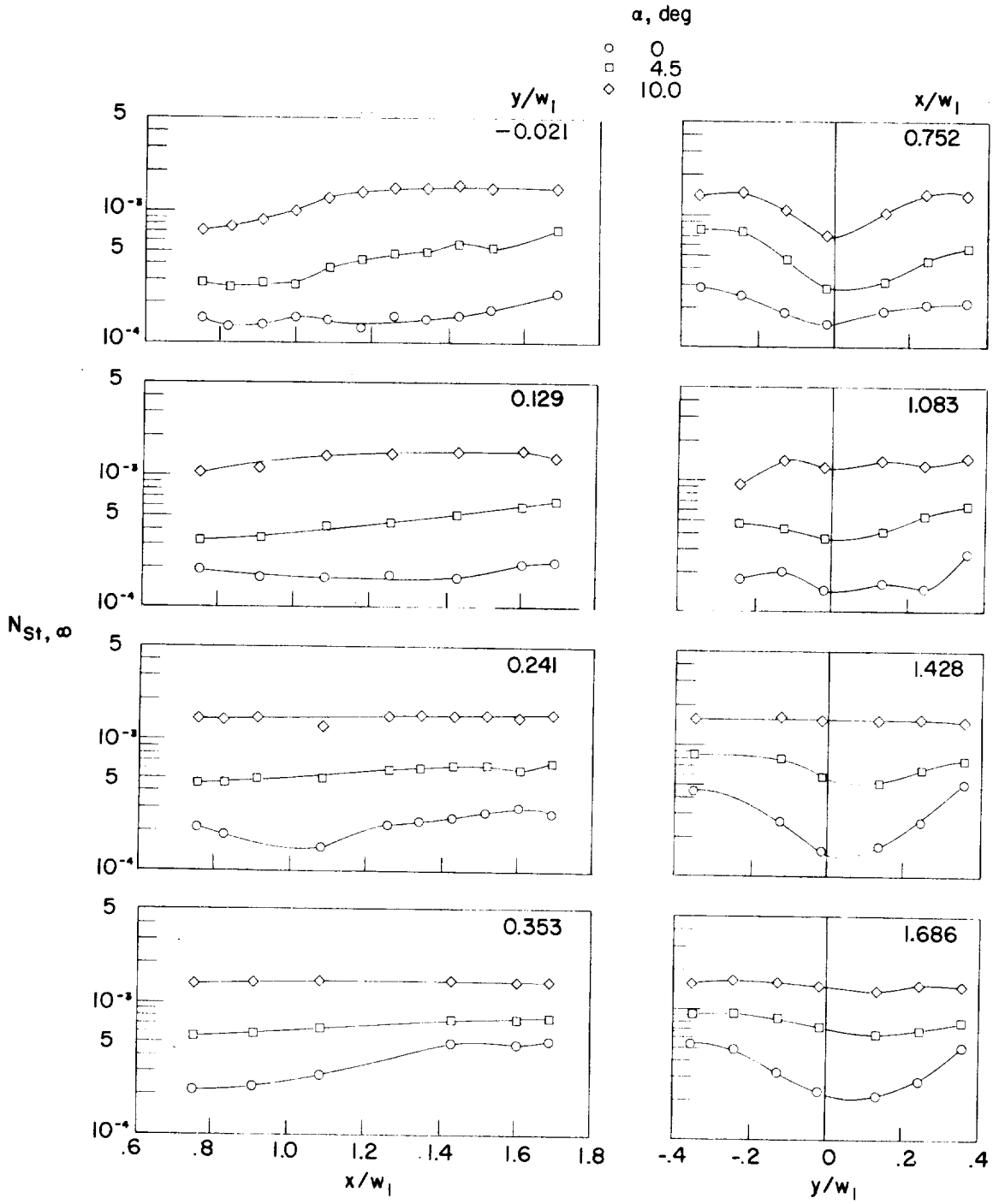

(c) $R_{L,\infty} = 3.3 \times 10^6$ per meter (1.0×10^6 per foot).

Figure 11.- Continued.

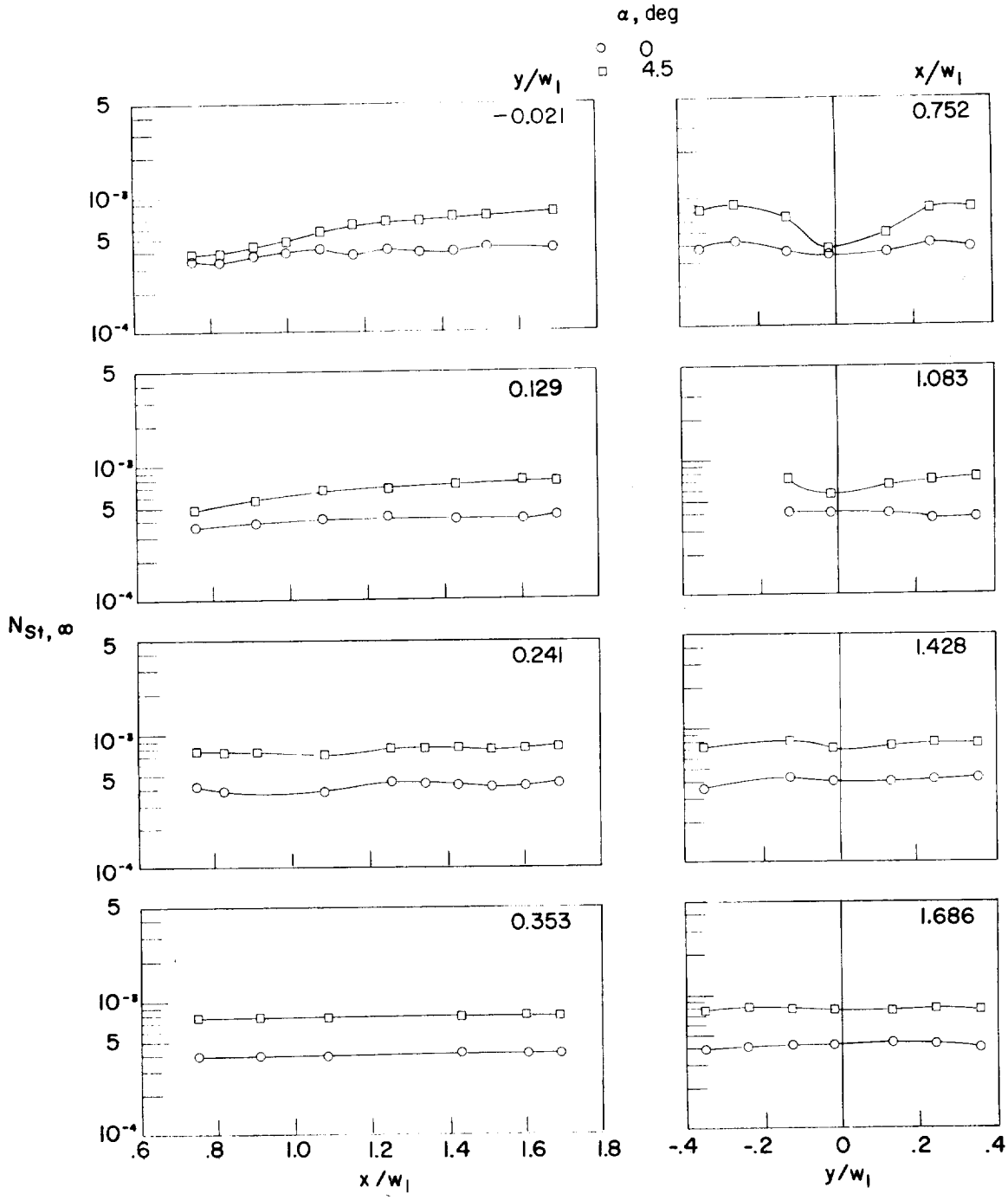

(d) $R_{L,\infty} = 4.9 \times 10^6$ per meter (1.5×10^6 per foot).

Figure 11.- Concluded.

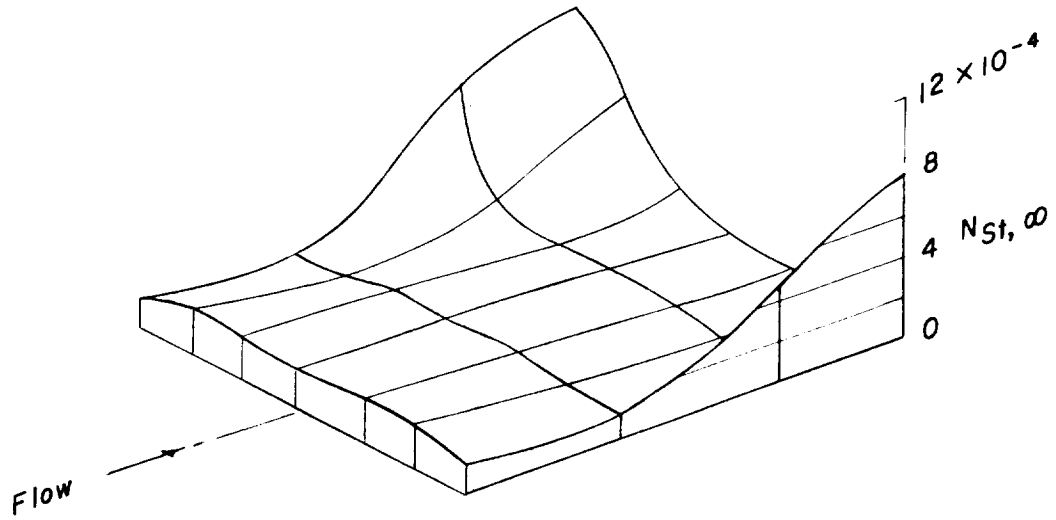

(a) $\alpha = 0^{o}$.

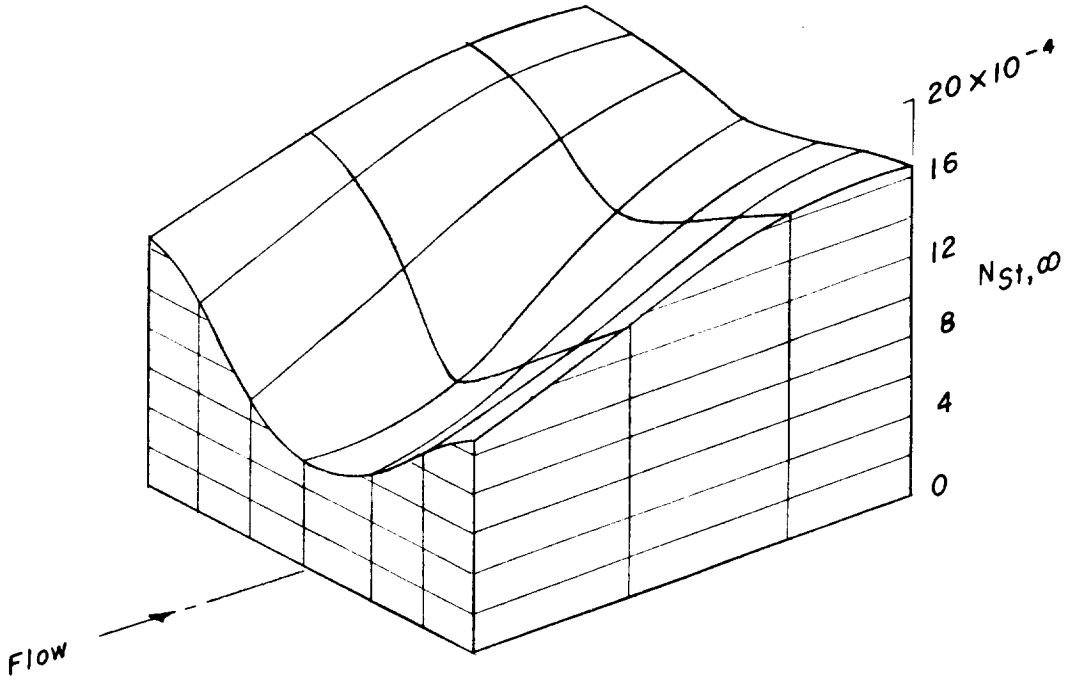

(b) $\alpha = 10^{o}$.

Figure 12.- Heat-transfer distributions on flat panel with blunt leading edge and without aerodynamic fences at $R_{L,\infty} = 2.0 \times 10^{6}$ per meter (0.6×10^{6} per foot) and $M_{\infty} = 7$.

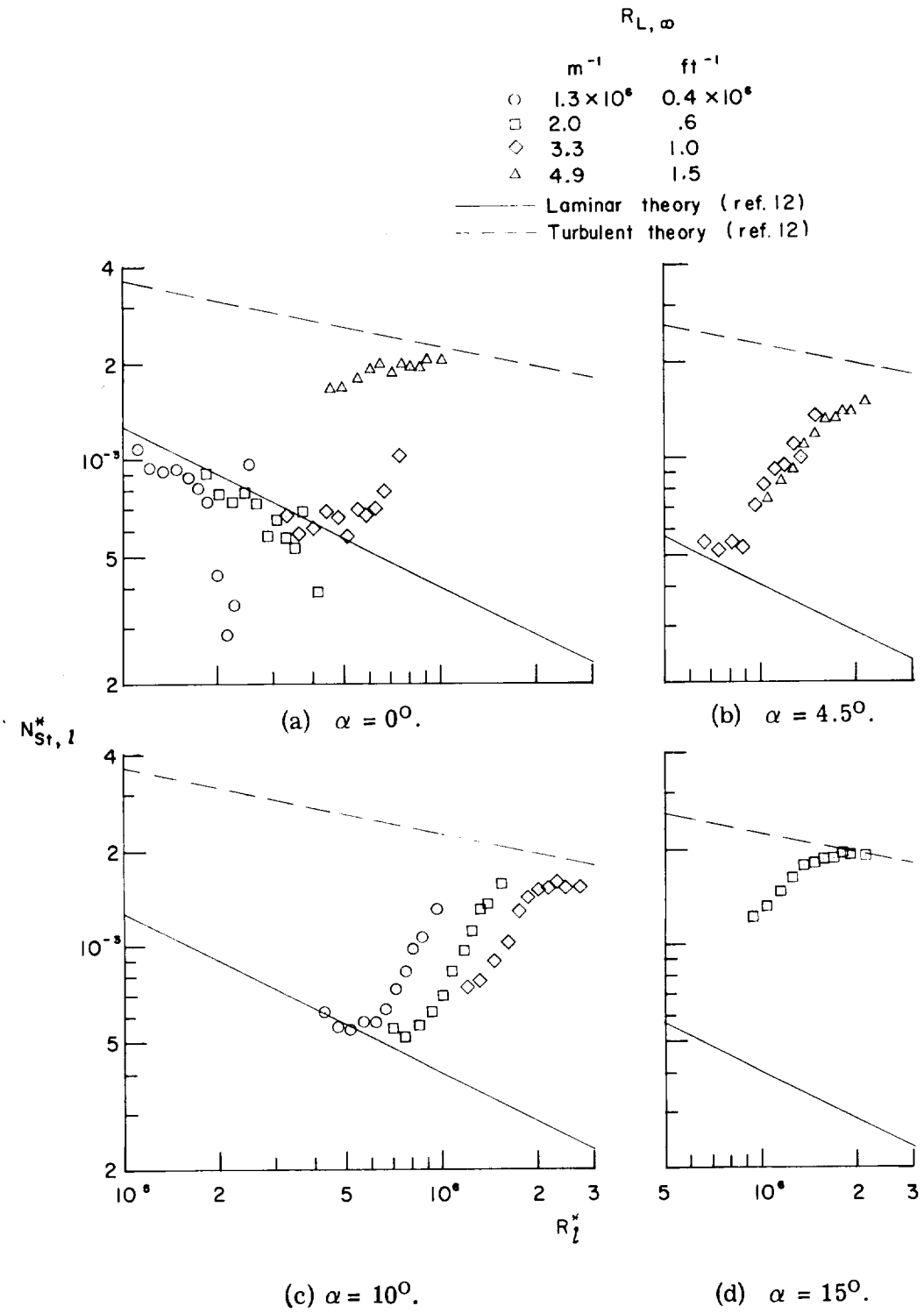

Figure 13.- Center-line cold-wall heat-transfer distributions on flat panel with blunt leading edge at $M_\infty = 7$.

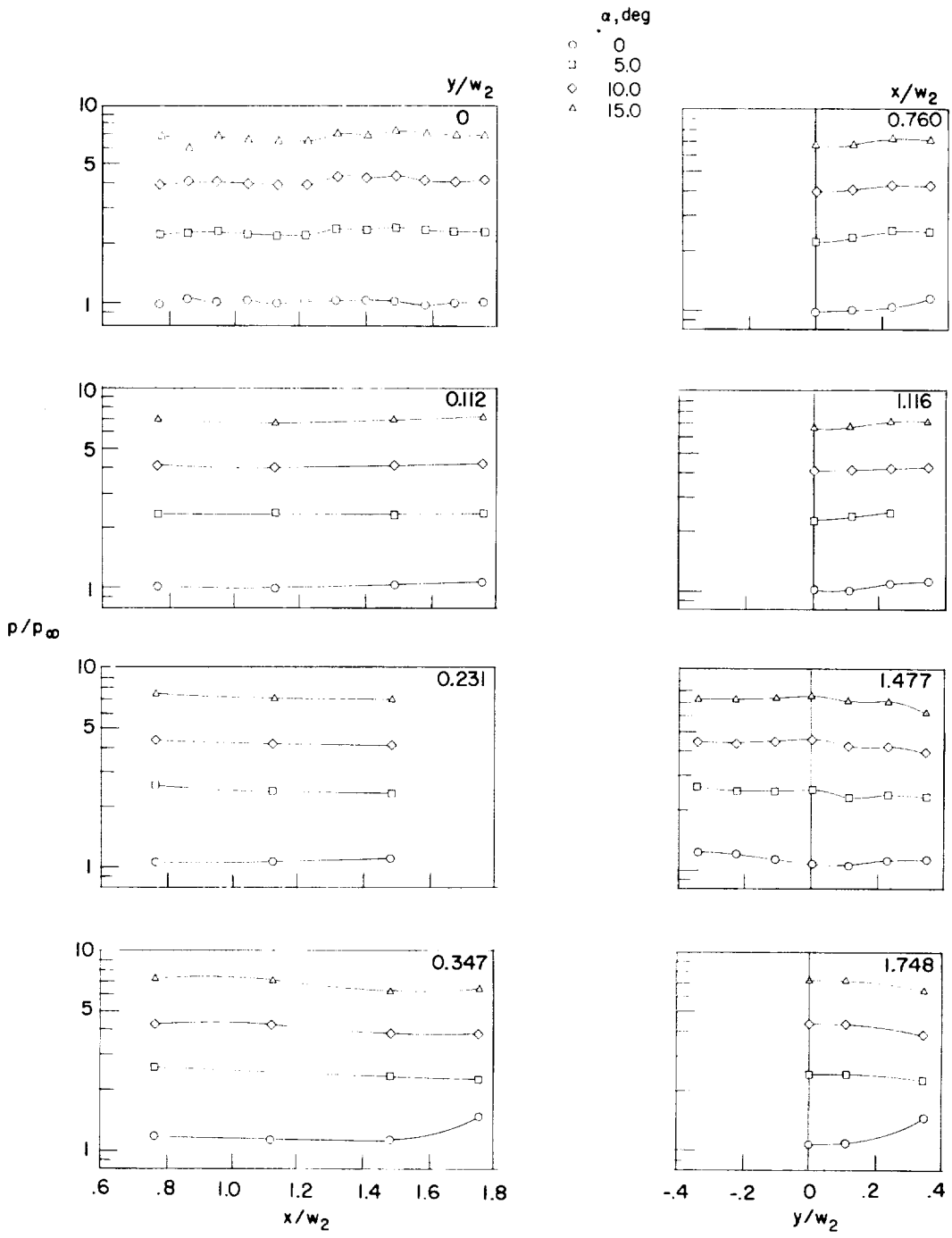

(a) $R_{L,\infty} = 2.0 \times 10^6$ per meter (0.6×10^6 per foot).

Figure 14.- Longitudinal and spanwise pressure distributions on flat panel with sharp leading edge, 0.24-cm-diameter (0.094-in.) boundary-layer flow trips, and aerodynamic fences at $M_\infty = 7$.

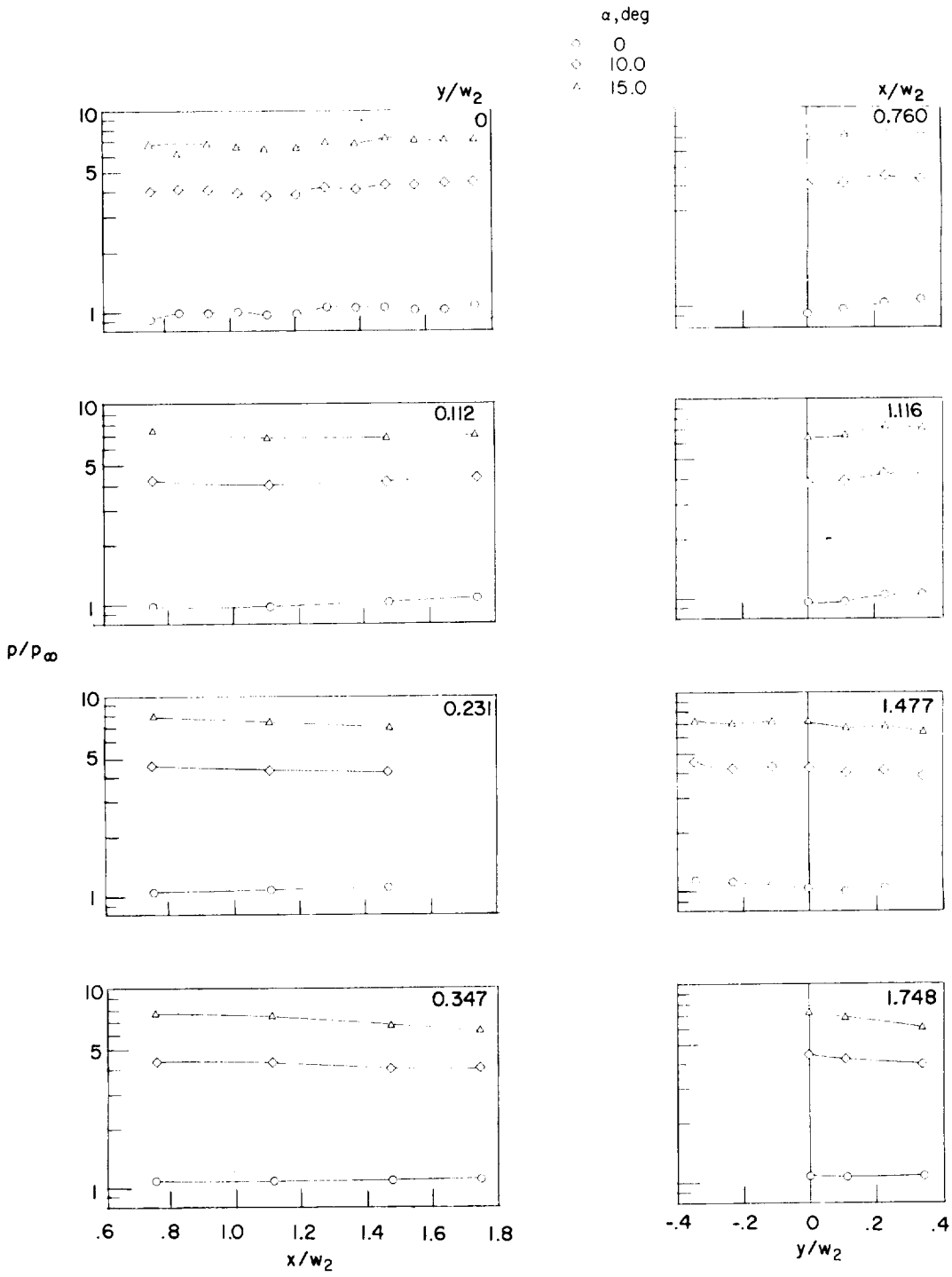

(b) $R_{L,\infty} = 3.3 \times 10^6$ per meter (1.0×10^6 per foot).

Figure 14.- Continued.

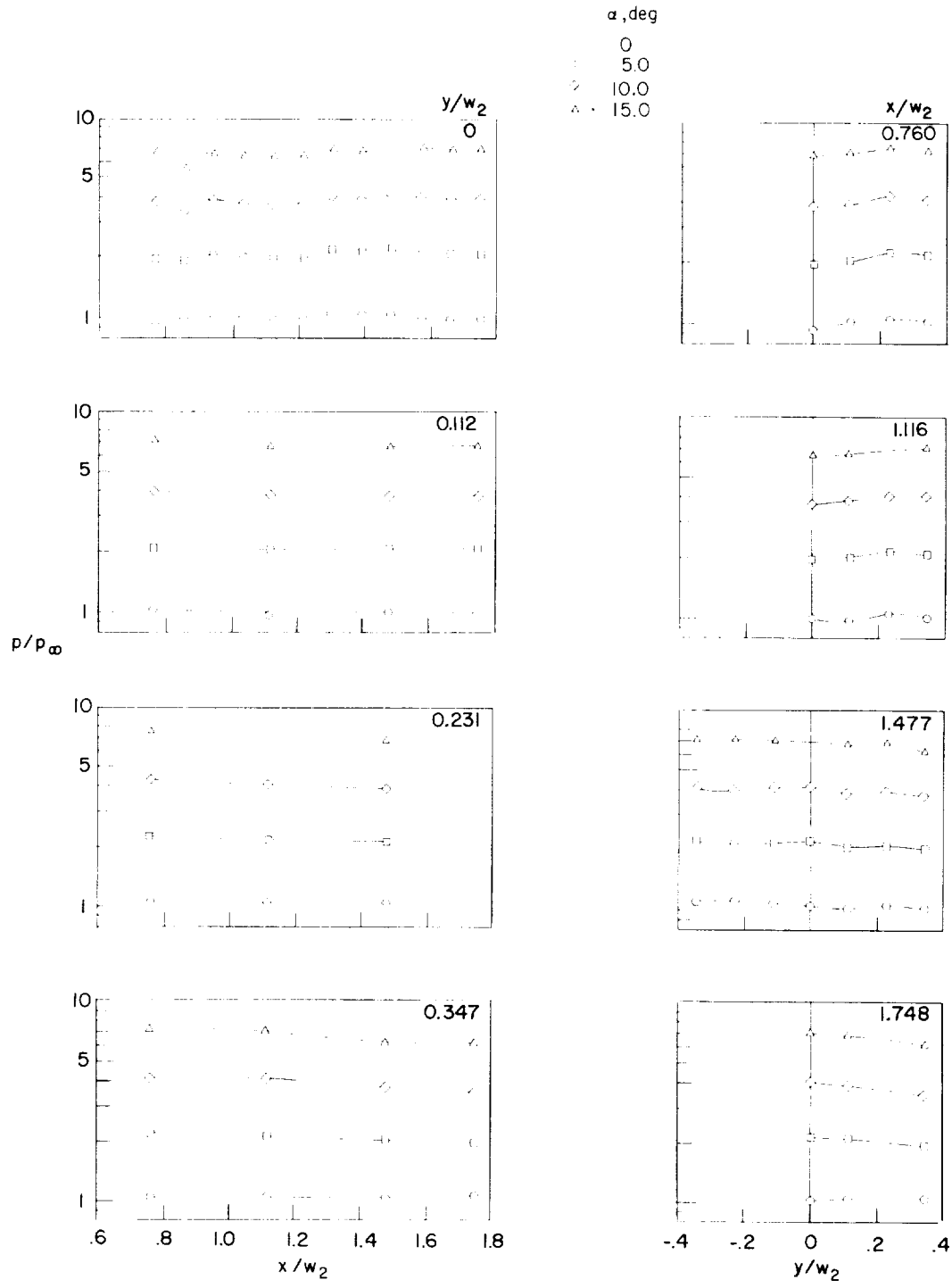

(c) $R_{L,\infty} = 4.9 \times 10^6$ per meter (1.5×10^6 per foot).

Figure 14.- Concluded.

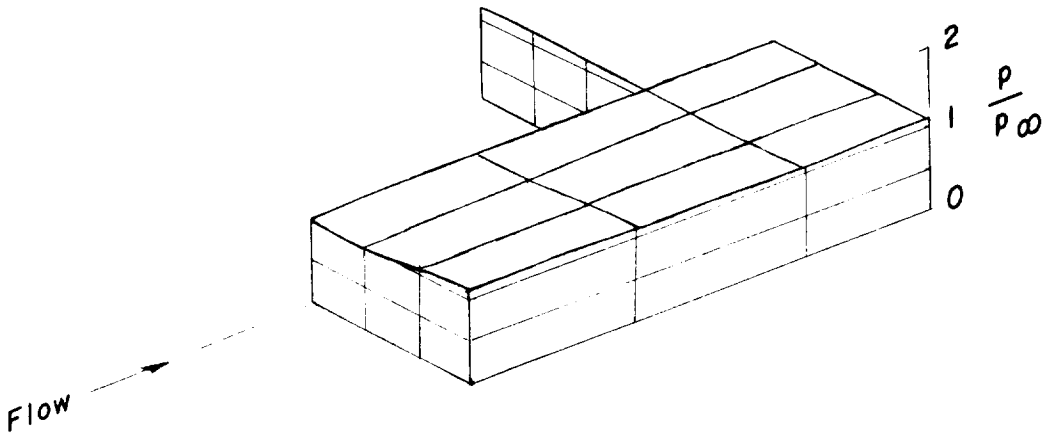

(a) $\alpha = 0^{o}$.

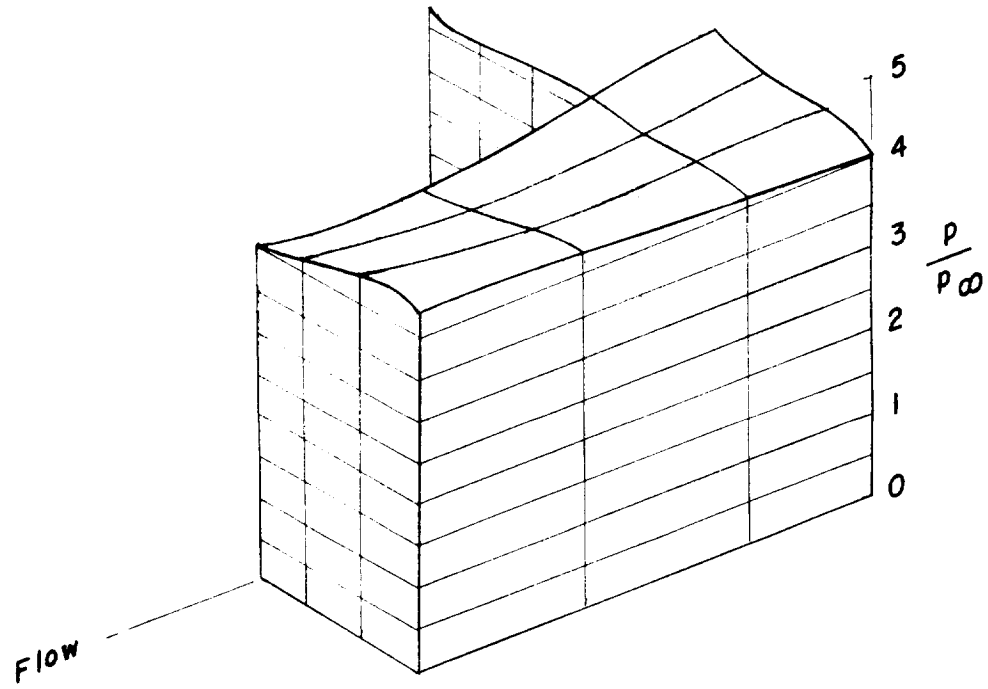

(b) $\alpha = 10^{o}$.

Figure 15.- Pressure distributions on flat panel with sharp leading edge, 0.24-cm-diameter (0.094-in.) boundary-layer flow trips, aerodynamic fences at $R_{L,\infty} = 3.3 \times 10^{6}$ per meter (1.0×10^{6} per foot), and $M_{\infty} = 7$.

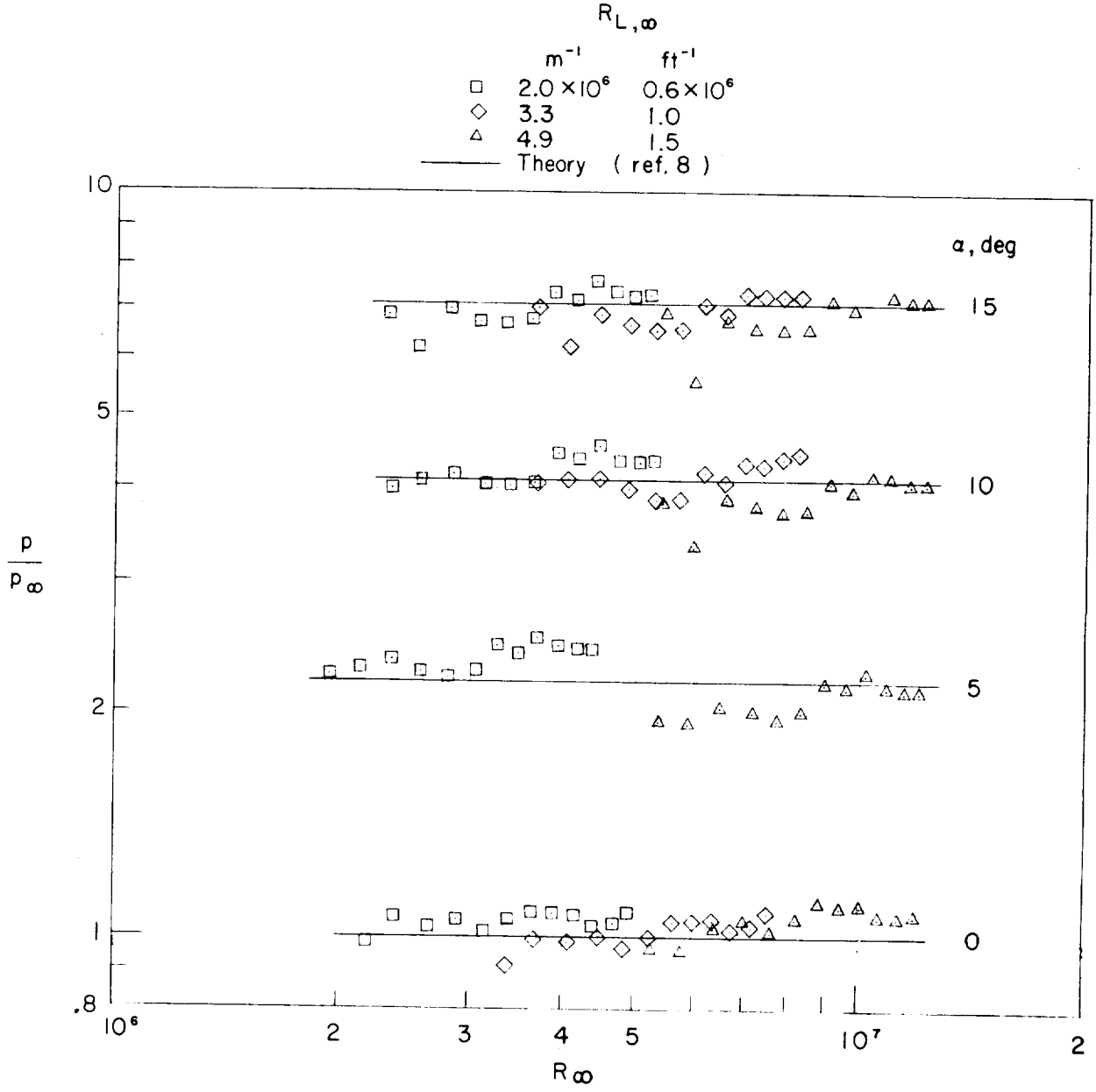

Figure 16.- Center-line pressure distribution along flat-panel surface with sharp leading edge, 0.24-cm-diameter (0.094-in.) boundary-layer flow trips, and aerodynamic fences at $M_\infty = 7$.

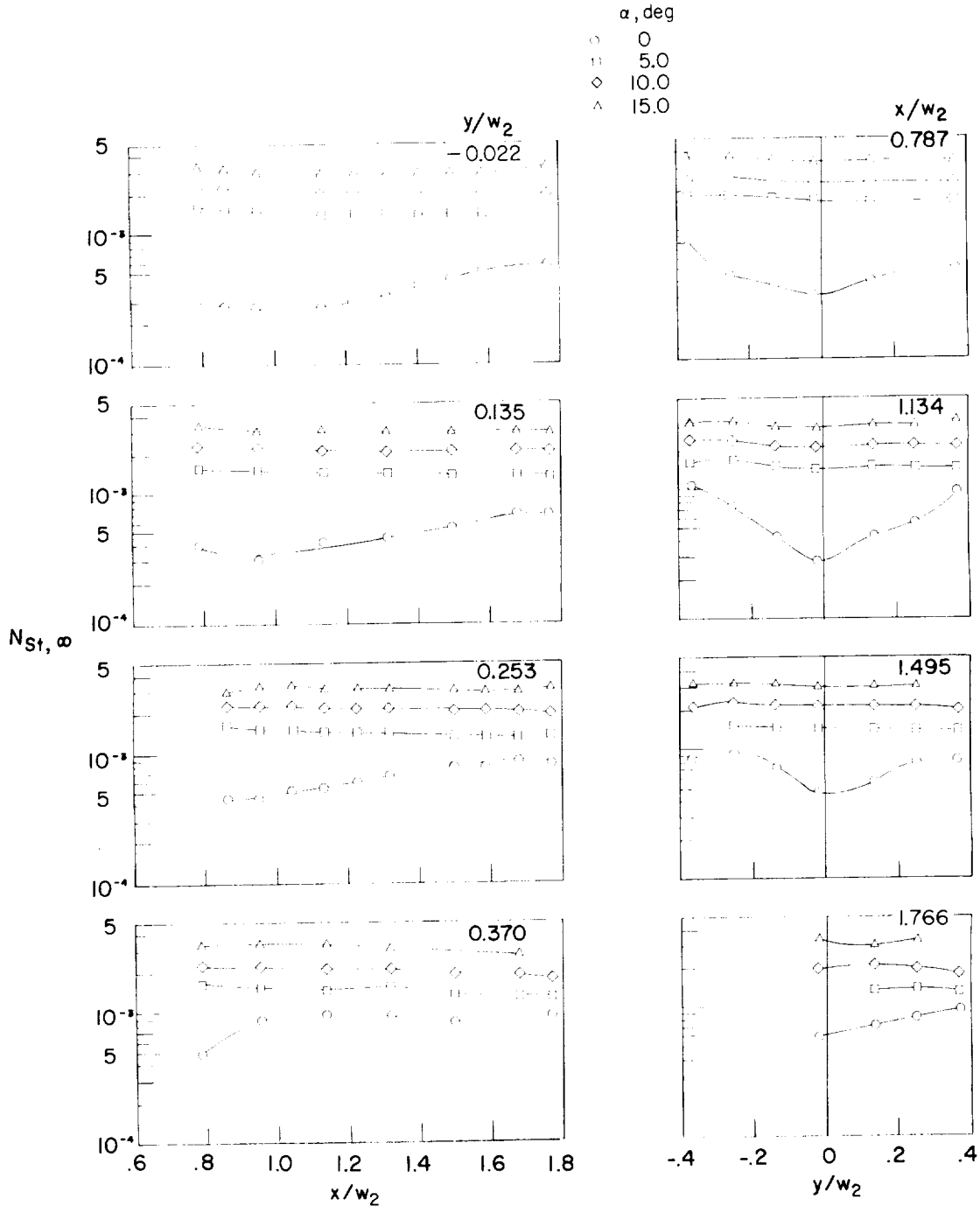

(a) $R_{L,\infty} = 2.0 \times 10^6$ per meter (0.6×10^6 per foot).

Figure 17.- Longitudinal and spanwise cold-wall heat-transfer distributions on flat panel with sharp leading edge, 0.24-cm-diameter (0.094-in.) boundary-layer flow trips, and aerodynamic fences at $M_\infty = 7$.

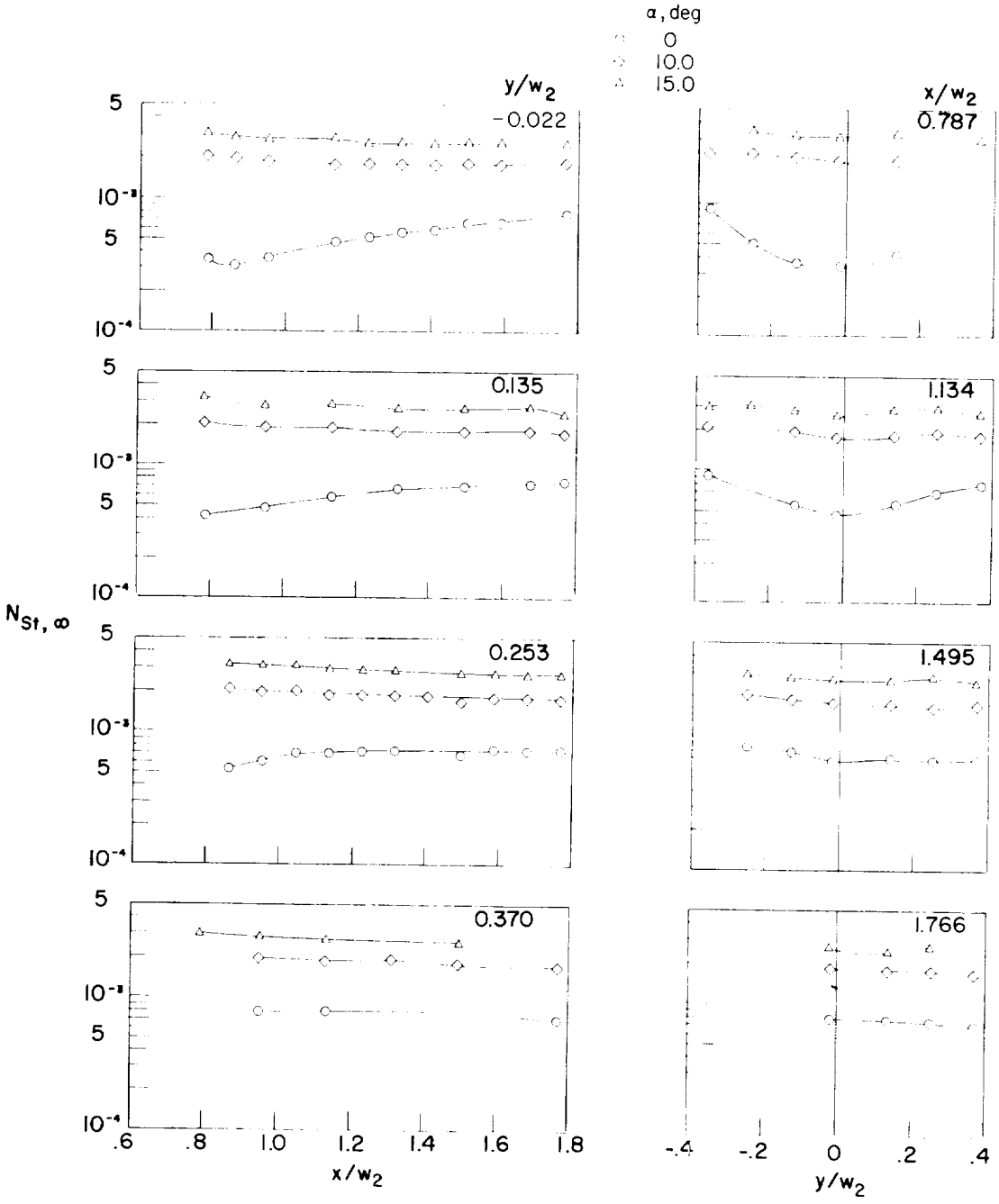

(b) $R_{L,\infty} = 3.3 \times 10^6$ per meter (1.0×10^6 per foot).

Figure 17.- Continued.

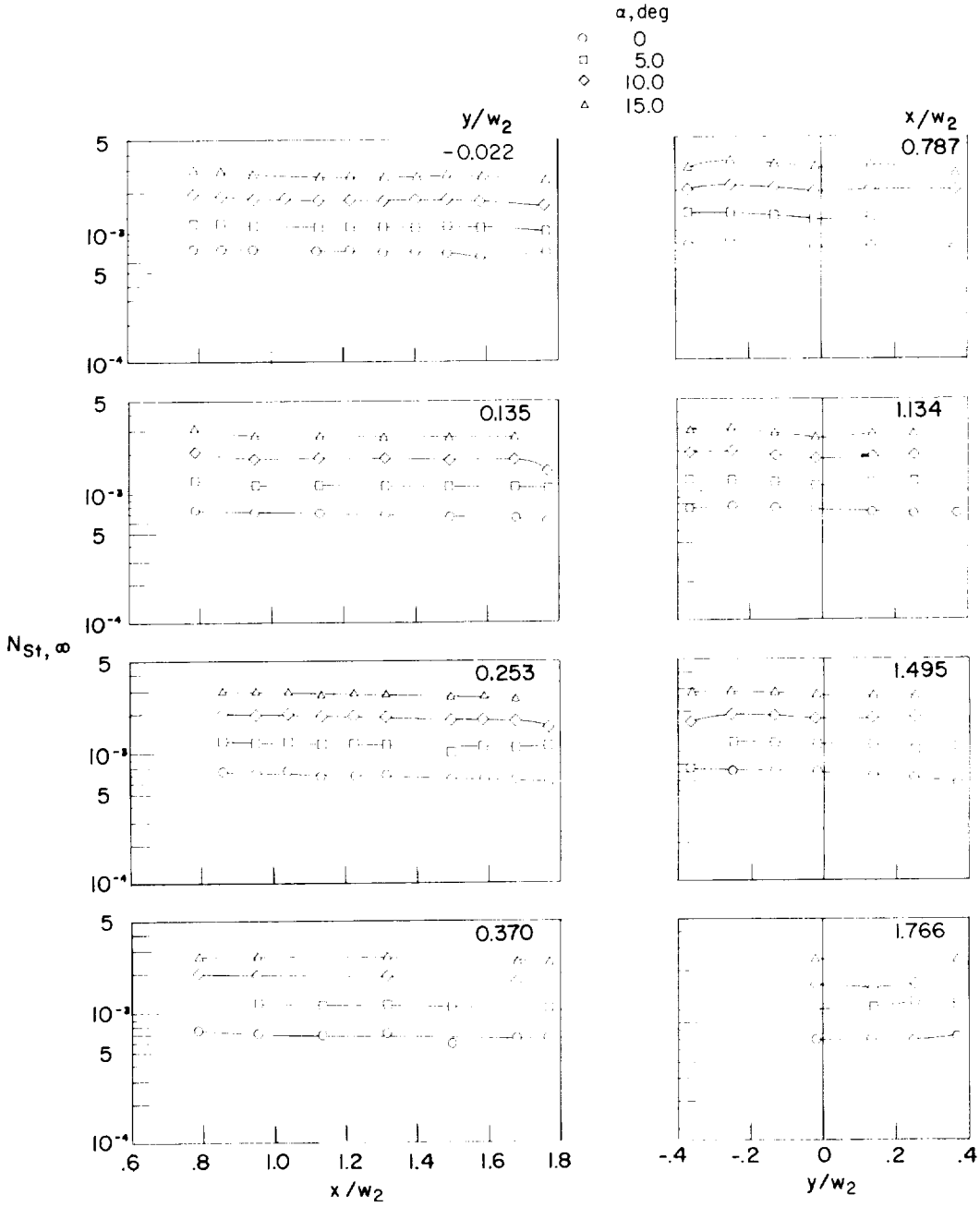

(c) $R_{L,\infty} = 4.9 \times 10^6$ per meter (1.5×10^6 per foot).

Figure 17.- Concluded.

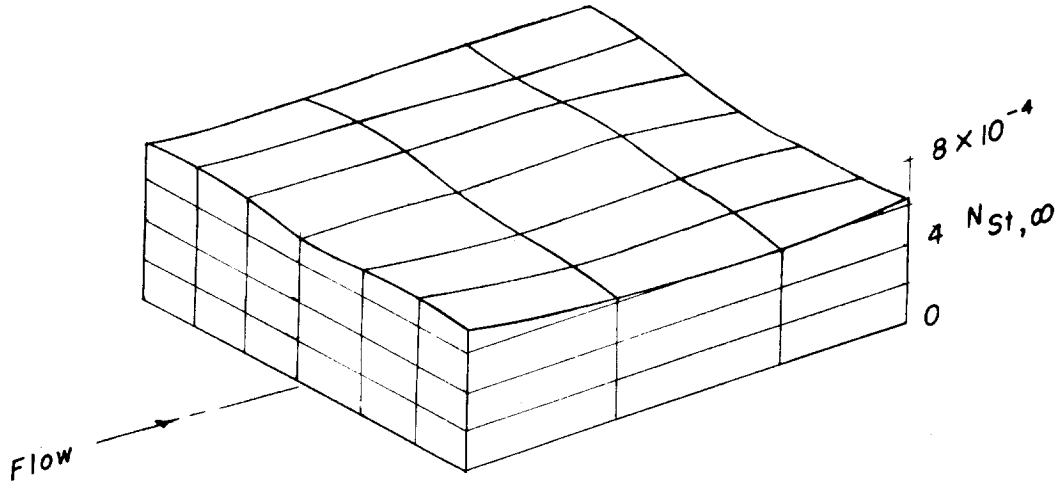

(a) $\alpha = 0^{o}$.

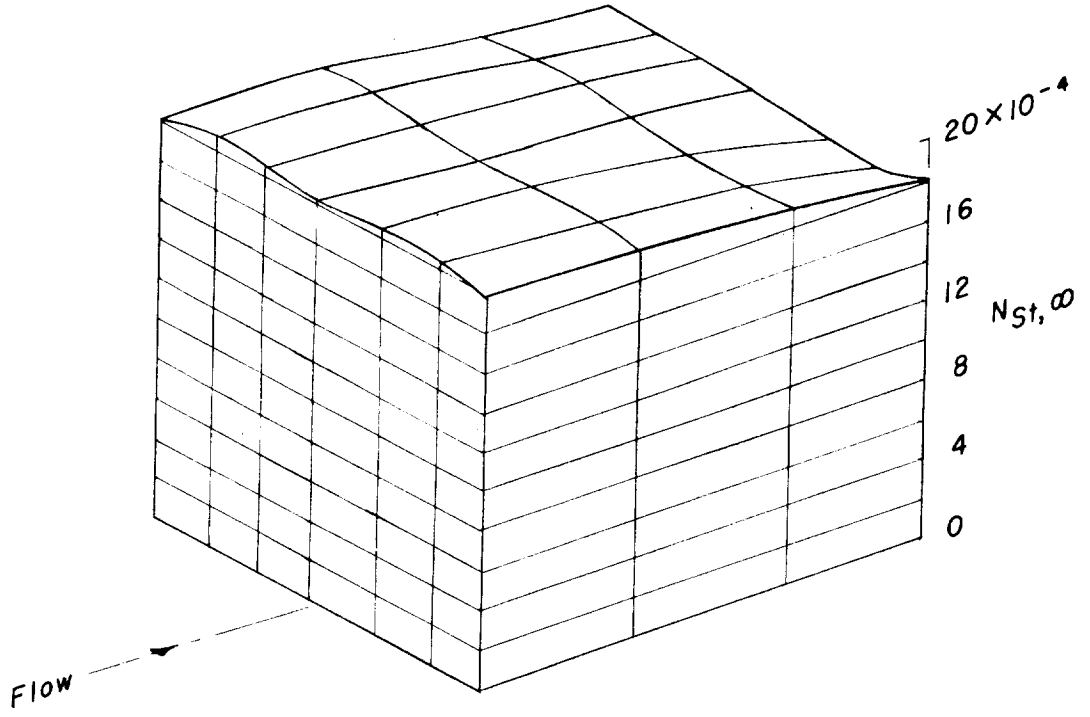

(b) $\alpha = 10^{o}$

Figure 18.- Heat-transfer distributions on flat panel with sharp leading edge, 0.24-cm-diameter (0.094-in.) boundary-layer flow trips, aerodynamic fences at $R_{L,\infty} = 4.9 \times 10^{6}$ per meter (1.5×10^{6} per foot), and $M_{\infty} = 7$.

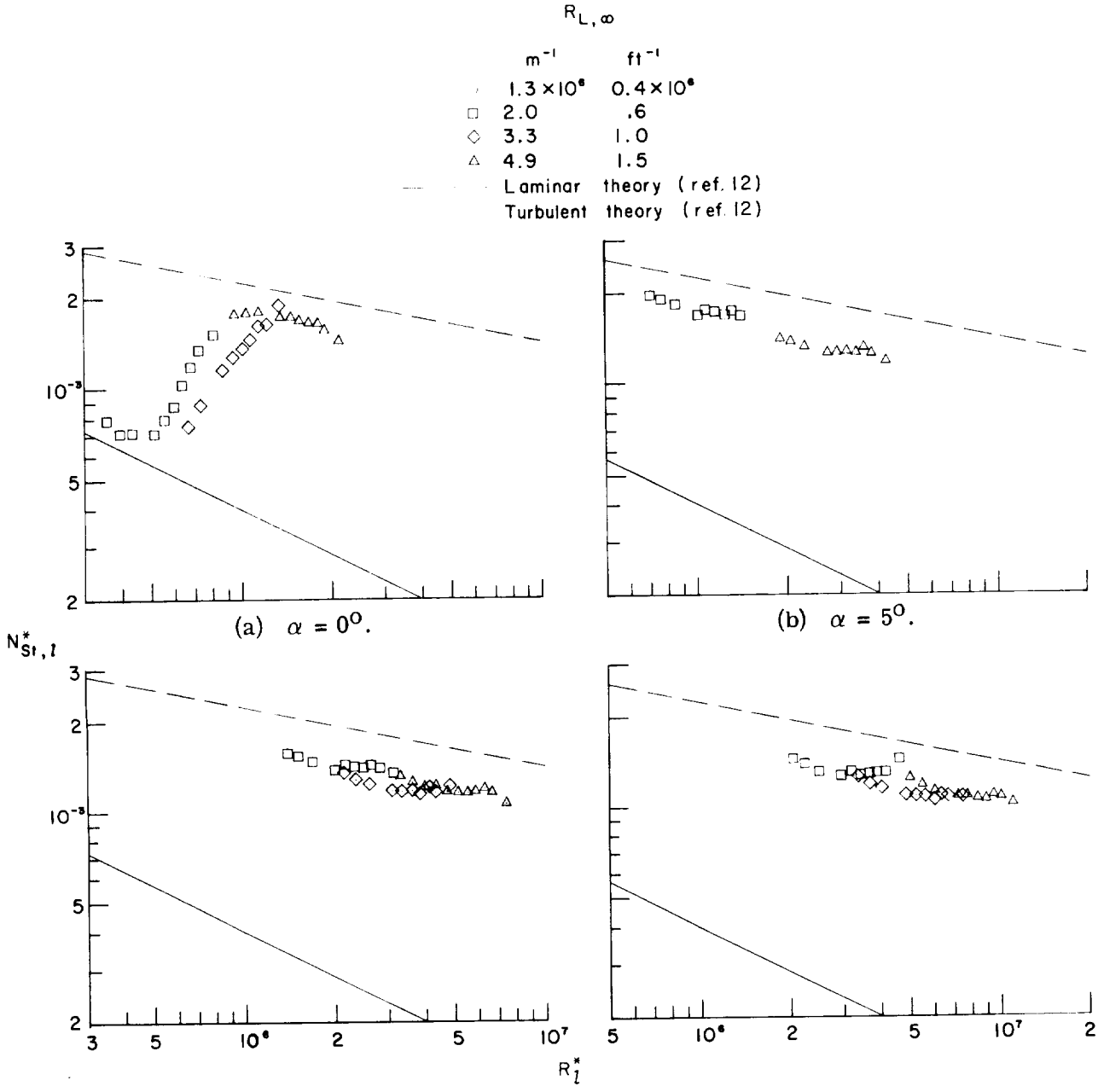

Figure 19.- Center-line cold-wall heat-transfer distributions on flat panel with sharp leading edge, 0.24-cm-diameter (0.094-in.) boundary-layer flow trips, and aerodynamic fences at $M_\infty = 7$.

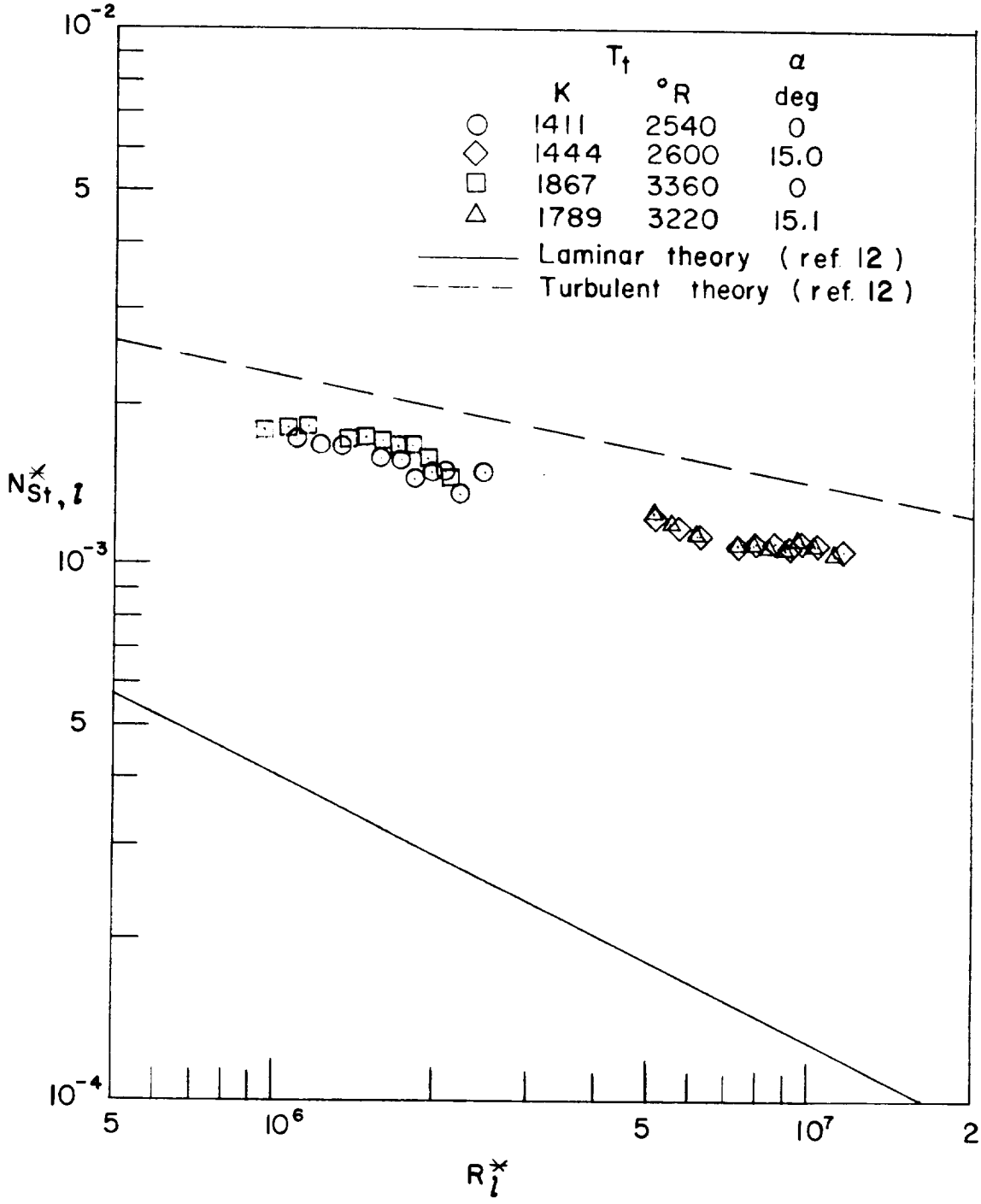

Figure 20.- Effects of stagnation temperature on cold-wall heat-transfer distributions on flat panel at $M_\infty = 7$.

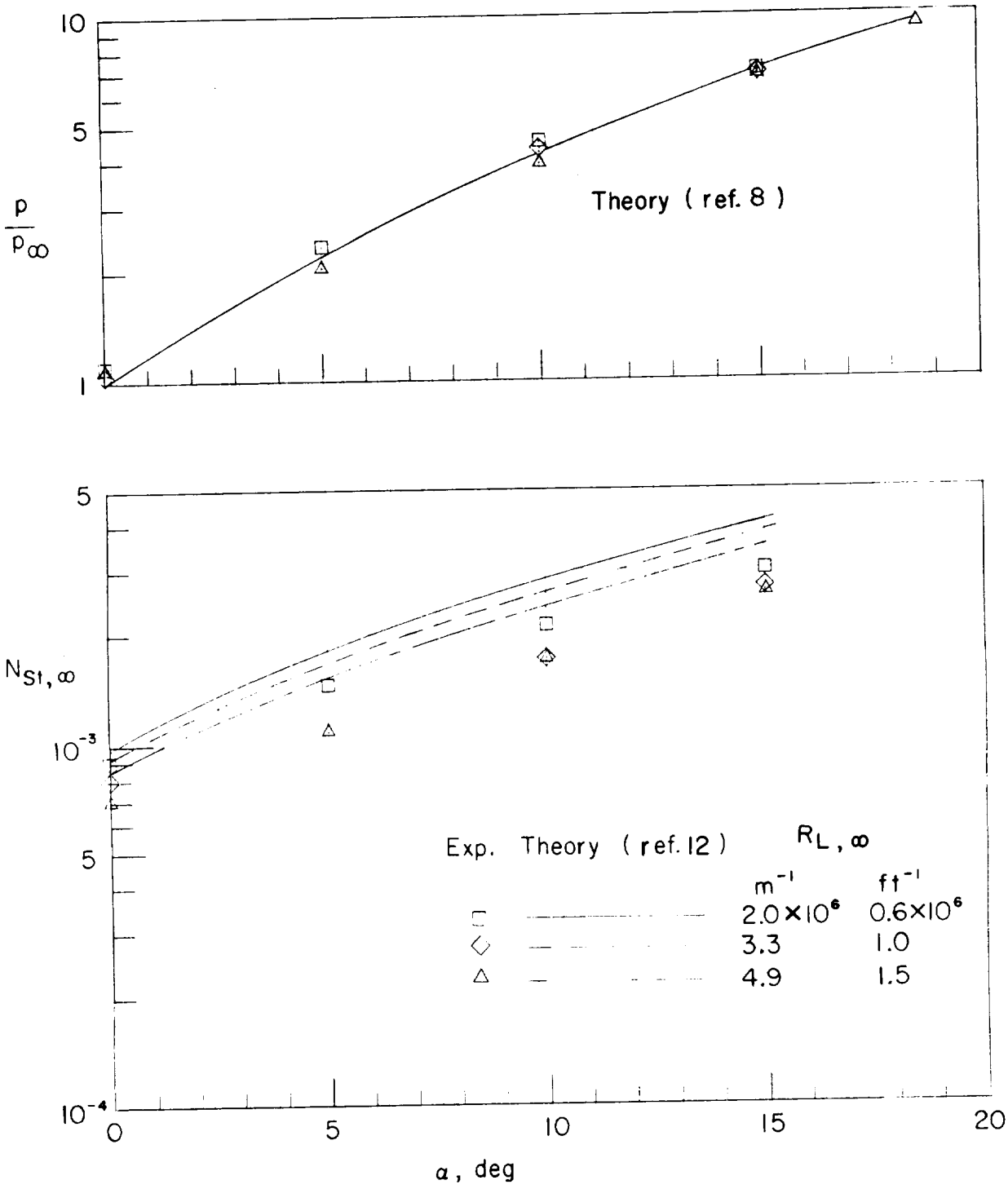

Figure 21.- Variation of average surface pressure ratio and cold-wall turbulent heat transfer with angle of attack on flat-panel surface at $M_\infty = 7$.

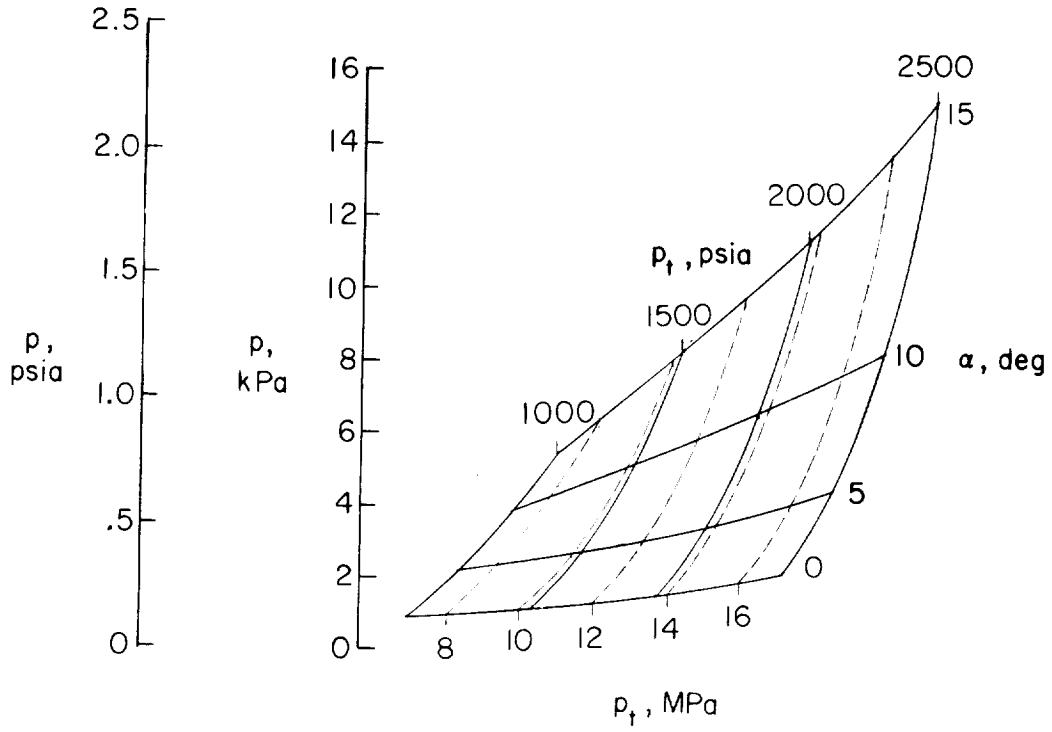

(a) Surface pressure.

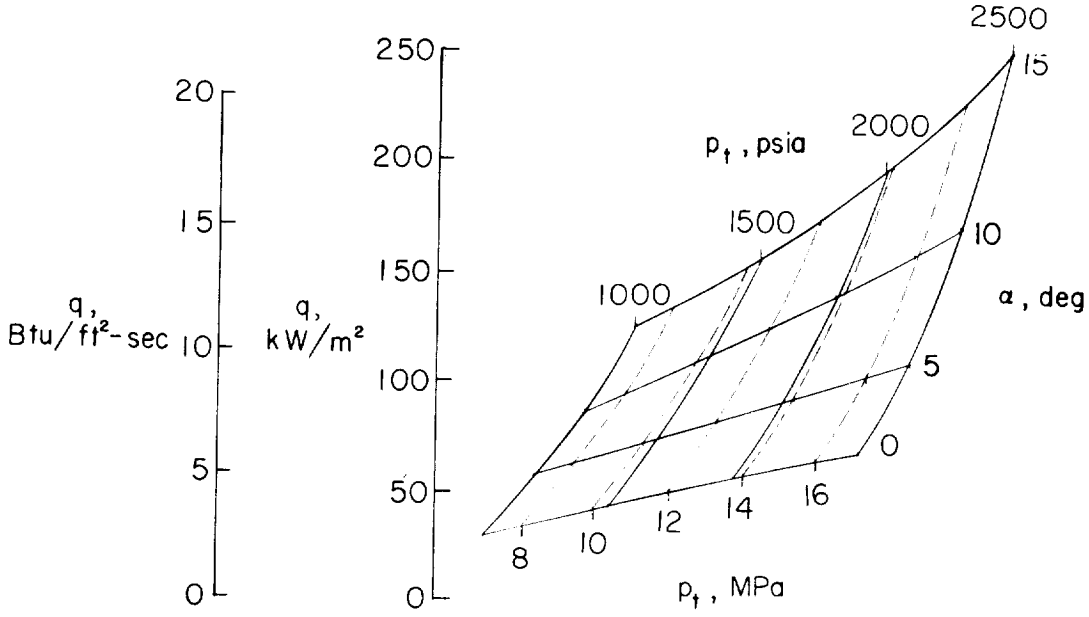

(b) Turbulent cold-wall heating rate.

Figure 22.- Carpet plots of average flat-plate surface pressures and cold-wall turbulent heating rates in the Langley 8-foot high-temperature structures tunnel. $M_\infty = 7$; $T_t = 1900$ K (3400° R).

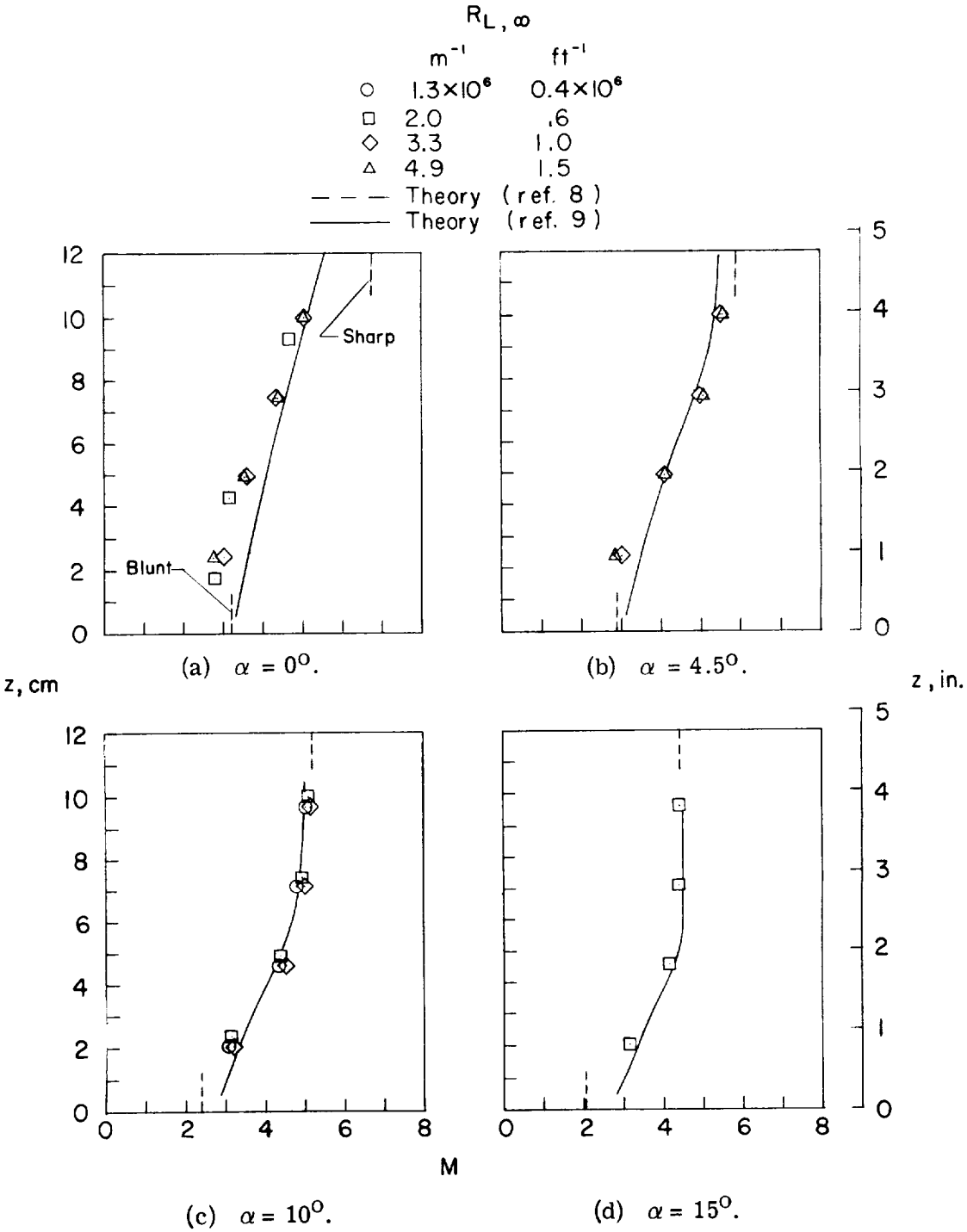

Figure 23.- Mach number distributions normal to panel-holder test surface with blunt leading edge from pitot static pressures measured at $x/w_1 = 1.76$; $M_\infty = 7$.

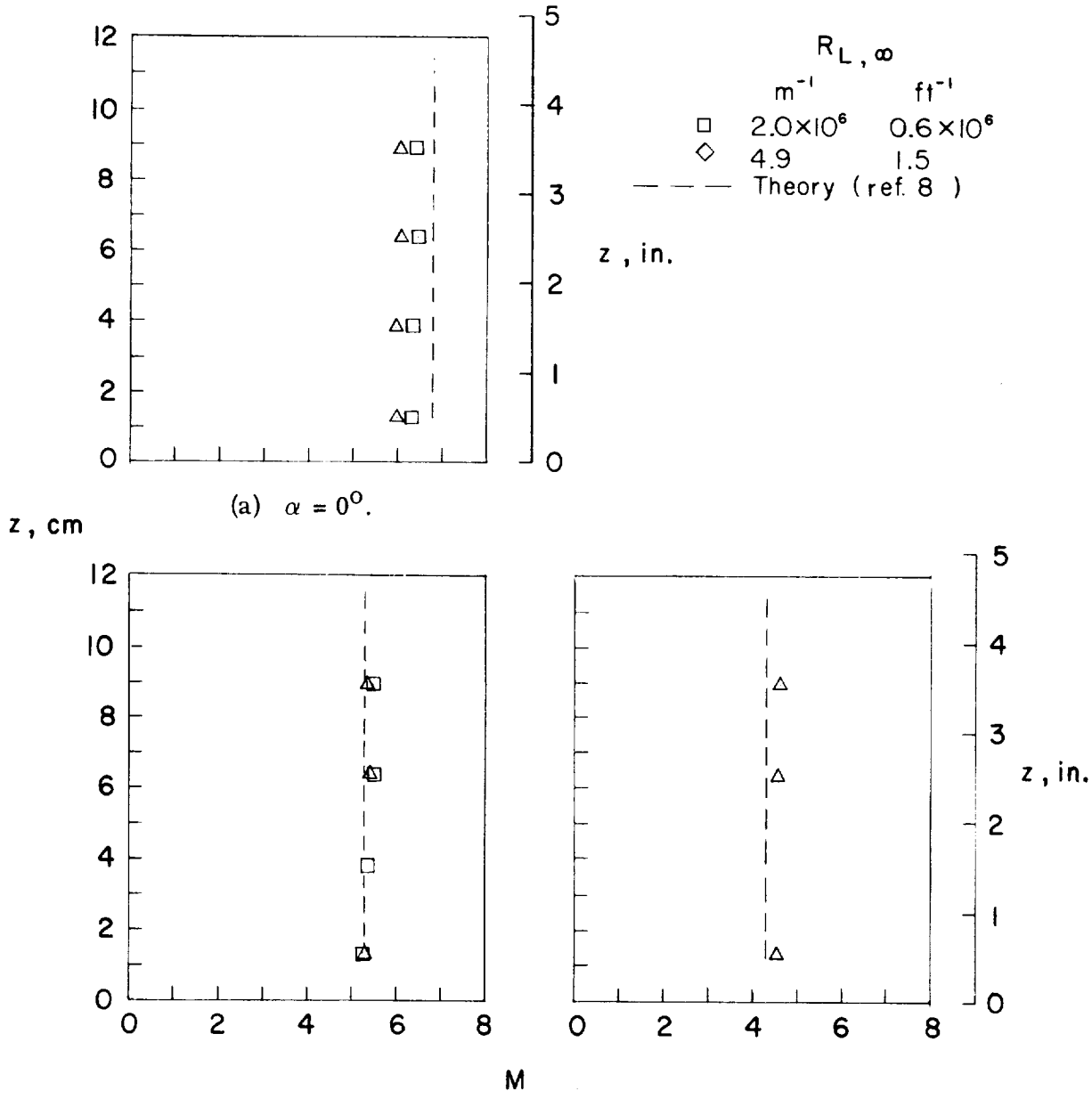

(a) $\alpha = 0^{o}$.

(b) $\alpha = 10^{o}$.

(c) $\alpha = 15^{o}$.

Figure 24.- Mach number distributions normal to panel-holder test surface with sharp leading edge from pitot static pressures measured at $x/w_2 = 1.85$; $M_\infty = 7$.

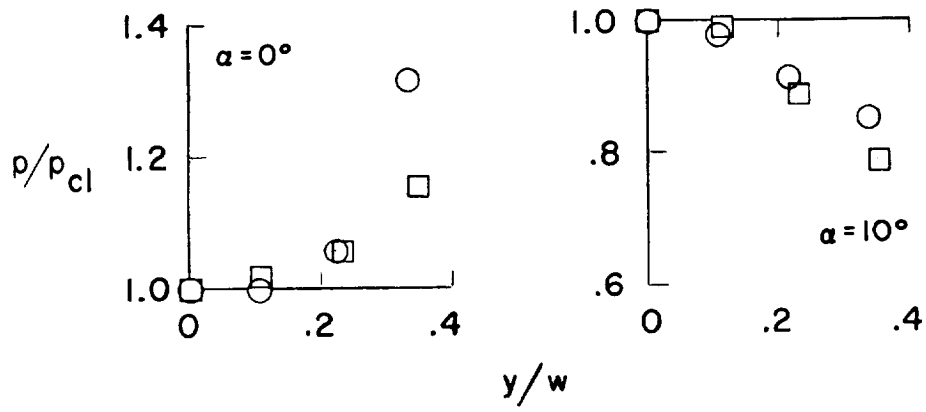

(a) $R_{L,\infty} = 2.0 \times 10^6$ per meter $(0.6 \times 10^6$ per foot).

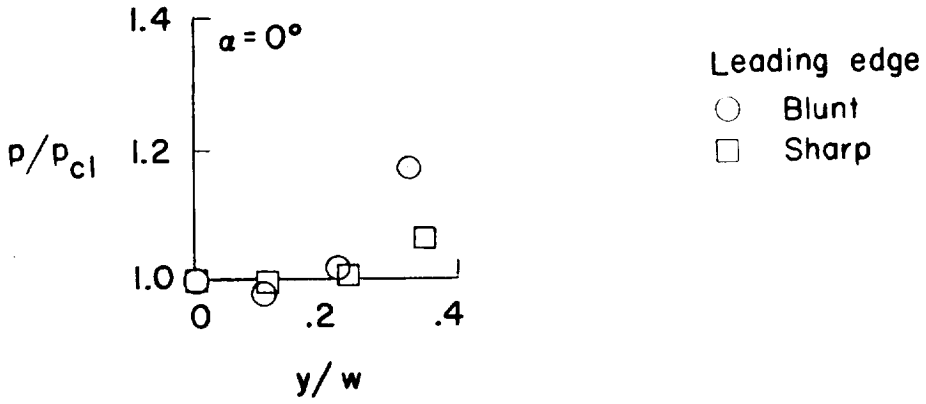

(b) $R_{L,\infty} = 4.9 \times 10^6$ per meter $(1.5 \times 10^6$ per foot).

Figure 25.- Effect of leading-edge bluntness on spanwise pressure distributions at trailing edge of flat panel at $M_\infty = 7$.

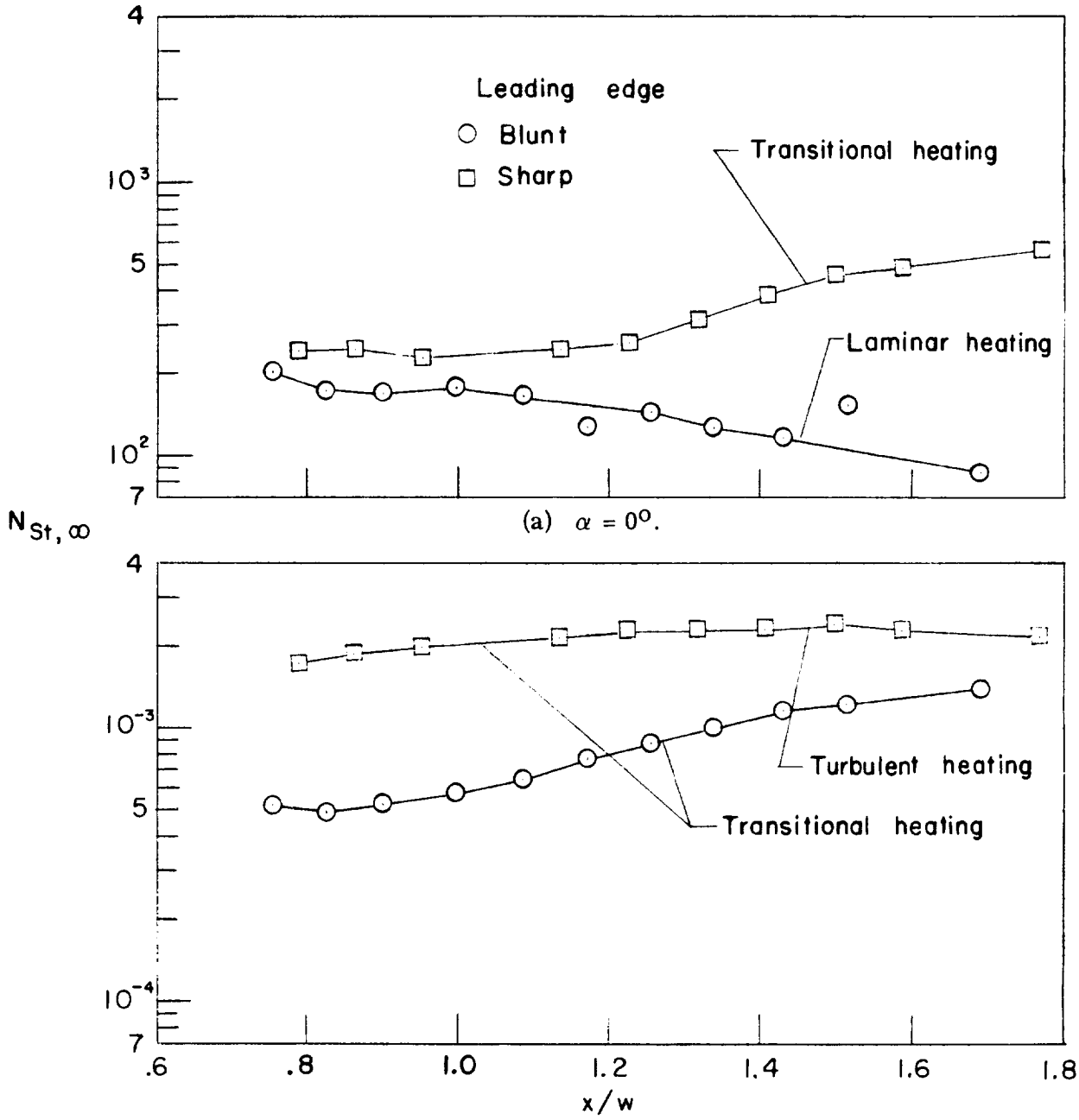

Figure 26.- Effect of leading-edge bluntness on center-line heat-transfer distributions on flat panel for $R_{L,\infty} = 2.0 \times 10^6$ per meter (0.6×10^6 per foot) at $M_\infty = 7$.

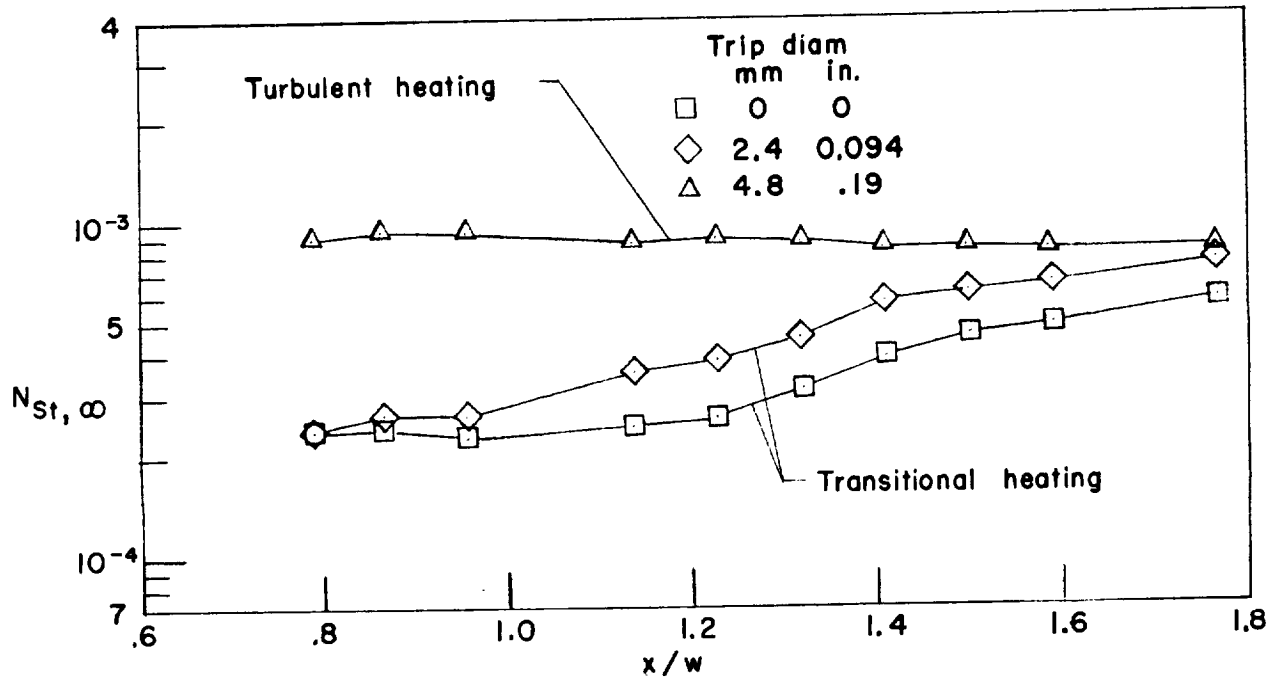

Figure 27.- Effect of boundary-layer flow trips on center-line cold-wall heat-transfer distributions on flat-panel surface for $\alpha = 0^{o}$ at $R_{L,\infty} = 2.0 \times 10^{6}$ per meter (0.6×10^{6} per foot) and $M_{\infty} = 7$.

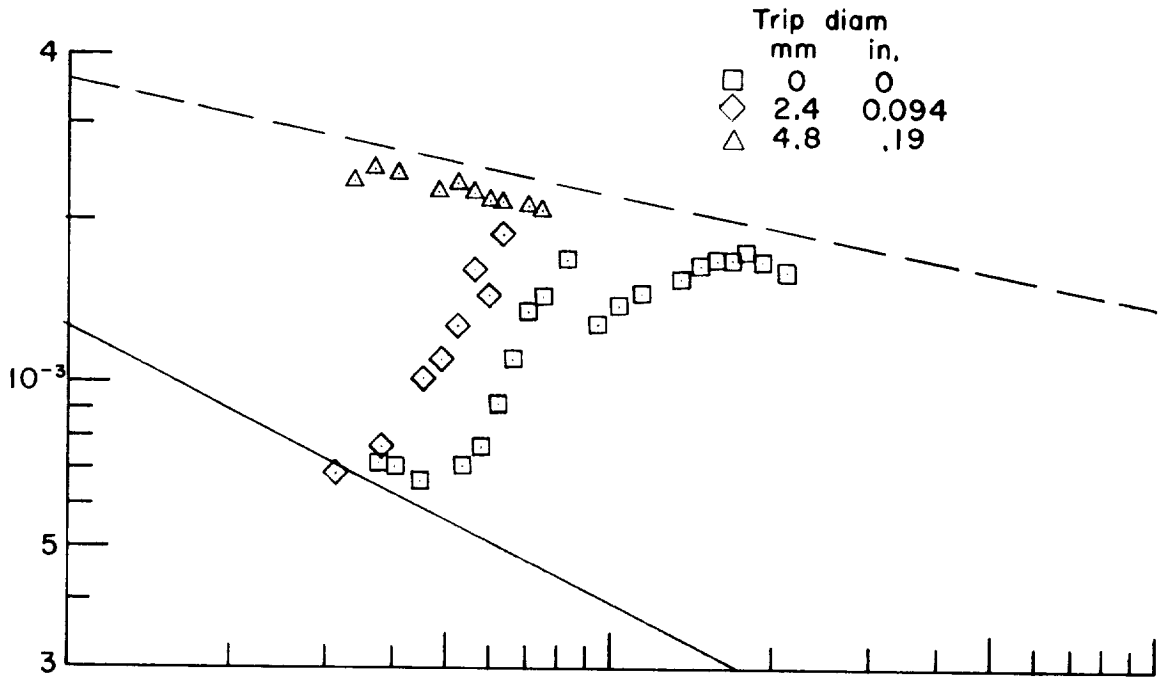

(a) $R_{L,\infty} = 2.0 \times 10^6$ per meter (0.6×10^6 per foot).

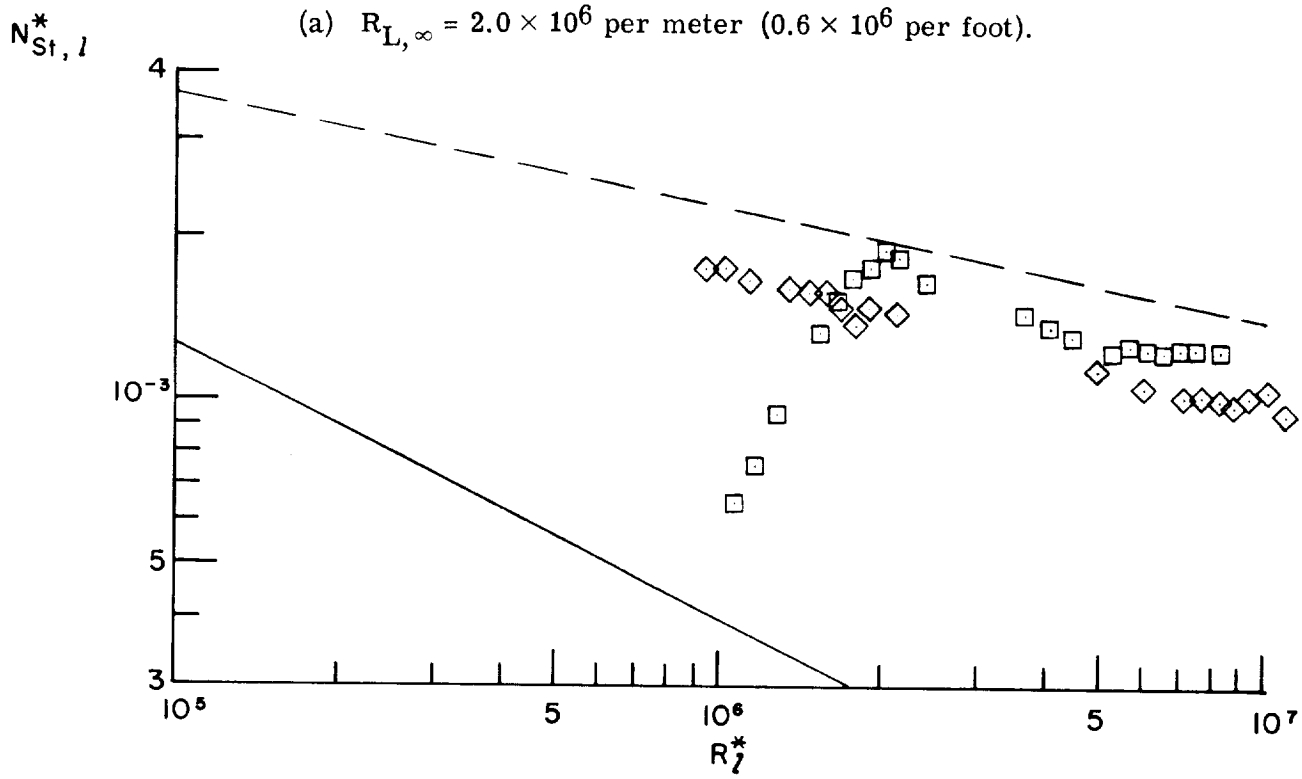

(b) $R_{L,\infty} = 4.9 \times 10^6$ per meter (1.5×10^6 per foot).

Figure 28.- Effect of boundary-layer flow trips on variation of center-line cold-wall Stanton number with local Reynolds number on flat panel at $M_\infty = 7$.

(a) $\alpha = 0^{o}$.

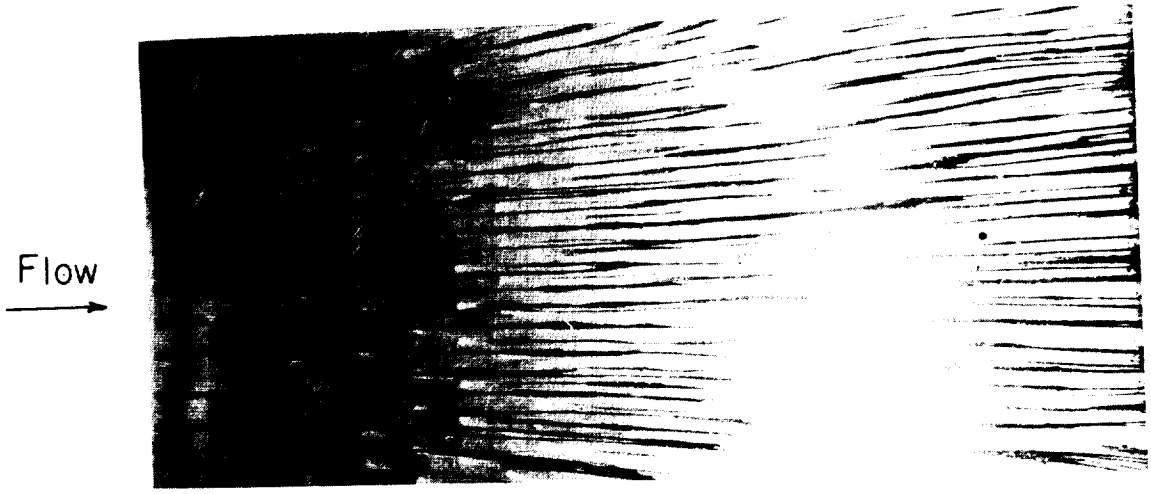

L-73-3067

(b) $\alpha = 10^{o}$.

Figure 29.- Oil-flow patterns on panel-holder test surface without aerodynamic fences at $M_{\infty} = 7$.

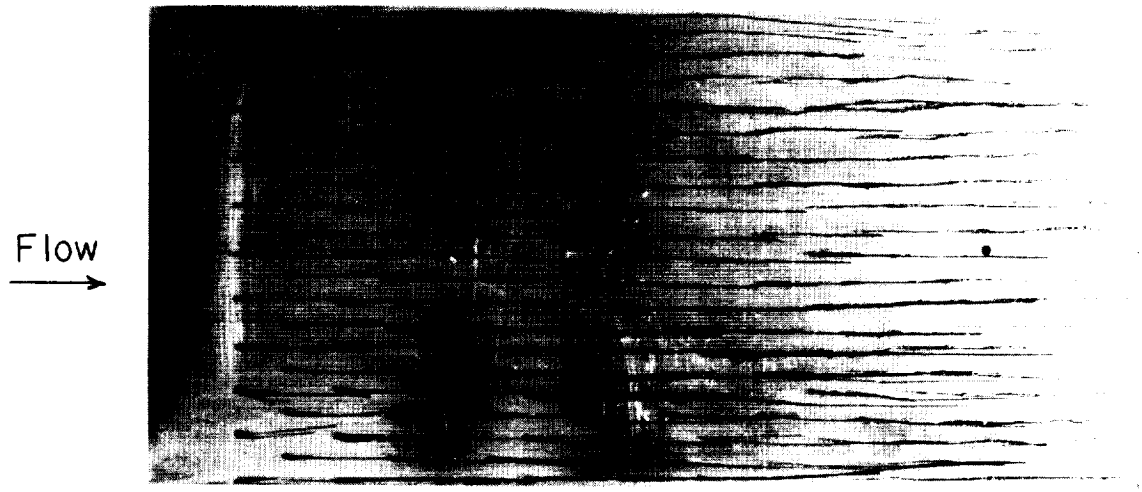

(a) $\alpha = 0^{o}$.

L-73-3068

(b) $\alpha = 10^{o}$.

Figure 30.- Oil-flow patterns on panel-holder test surface with aerodynamic fences at $M_{\infty} = 7$.

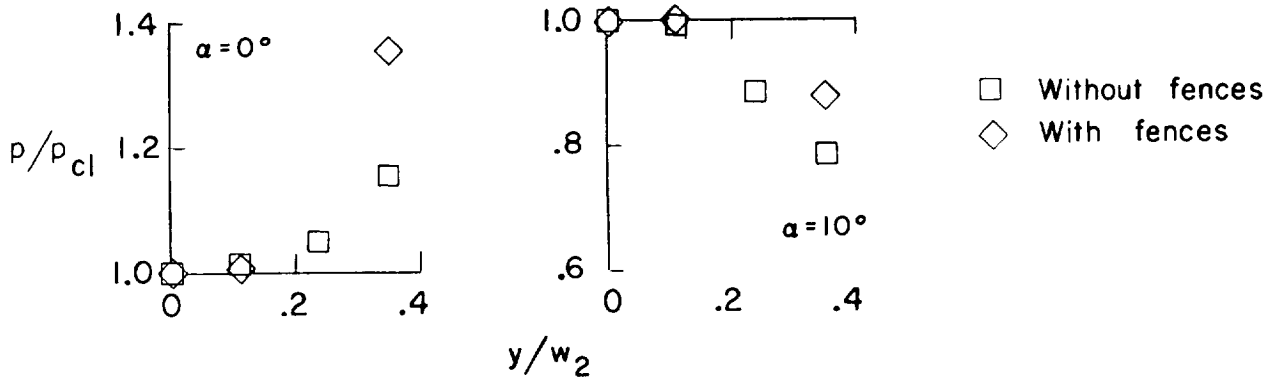

(a) $R_{L,\infty} = 2.0 \times 10^6$ per meter $(0.6 \times 10^6$ per foot).

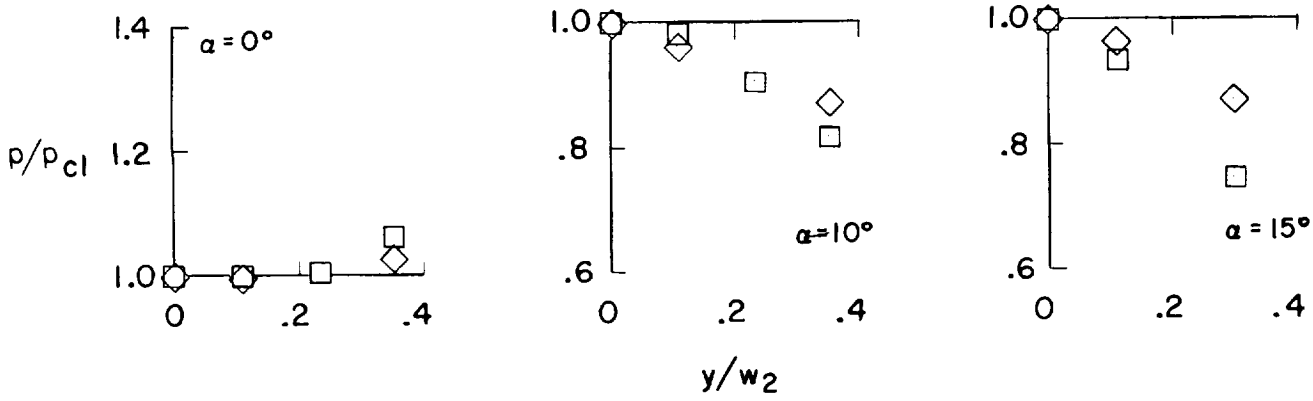

(b) $R_{L,\infty} = 4.9 \times 10^6$ per meter $(1.5 \times 10^6$ per foot).

Figure 31.- Effect of aerodynamic fences on spanwise pressure distributions at trailing edge of flat panel. $(x/w_2 = 1.748;\ M_\infty = 7.)$